ACS OMEGA

http://pubs.acs.org/journal/acsodf

Perspective

# Metrics for Evaluation and Screening of Metal–Organic Frameworks for Applications in Mixture Separations

Rajamani Krishna*

Cite This: *ACS Omega* 2020, 5, 16987–17004

Read Online

ACCESS | Metrics & More | Article Recommendations | Supporting Information

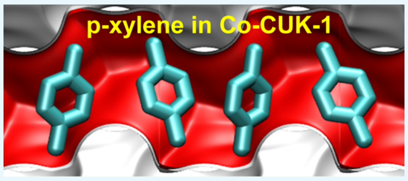

**ABSTRACT:** For mixture separations, metal–organic frameworks (MOFs) are of practical interest. Such separations are carried out in fixed bed adsorption devices that are commonly operated in a transient mode, utilizing the pressure swing adsorption (PSA) technology, consisting of adsorption and desorption cycles. The primary objective of this article is to provide an assessment of the variety of metrics that are appropriate for screening and ranking MOFs for use in fixed bed adsorbers. By detailed analysis of several mixture separations of industrial significance, it is demonstrated that besides the adsorption selectivity, the performance of a specific MOF in PSA separation technologies is also dictated by a number of factors that include uptake capacities, intracrystalline diffusion influences, and regenerability. Low uptake capacities often reduce the efficacy of separations of MOFs with high selectivities. A combined selectivity–capacity metric, $\Delta q$, termed as the separation potential and calculable from ideal adsorbed solution theory, quantifies the maximum productivity of a component that can be recovered in either the adsorption or desorption cycle of transient fixed bed operations. As a result of intracrystalline diffusion limitations, the transient breakthroughs have distended characteristics, leading to diminished productivities in a number of cases. This article also highlights the possibility of harnessing intracrystalline diffusion limitations to reverse the adsorption selectivity; this strategy is useful for selective capture of nitrogen from natural gas.

## 1. INTRODUCTION

During the last 2 decades, there has been a substantial increase in the development and synthesis of novel microporous crystalline materials for use as selective adsorbents in a variety of industrially important separation applications; examples of such materials include metal–organic frameworks (MOFs), zeolitic imidazolate frameworks (ZIFs), porous organic cages, porous aromatic frameworks, covalent organic frameworks, and polymers with intrinsic microporosity. Such separations are normally carried out in fixed bed devices that are operated in a transient mode, consisting of adsorption and desorption cycles. In one class of applications, the motivation has been to afford energy-efficient and environmentally benign alternatives to conventional separations such as absorption, distillation, extraction, or crystallization. In other cases, there are incentives for enhancing the separation performance by replacing the currently used microporous adsorbents such as cation-exchanged zeolites and activated carbon (AC) with tailor-made MOFs. To set the scene and define the objectives of this article, we consider a number of mixture separations that may be targeted for the development of novel MOFs.

Arguably, the most important and successful industrial application of adsorption separations is for $H_2$ purification. The catalytic reforming of natural gas, when combined with a water gas shift reaction step, yields a hydrogen-rich product stream containing a number of impurities such as $H_2O$ vapor, $CO_2$, $CH_4$, CO, and $N_2$.[1−3] These impurities must be removed in order to attain the 99.95%+ $H_2$ purity that is normally demanded.[1] In fuel cell applications, the purity demands are as high as 99.99%+.[2,4] Large-scale production of hydrogen, with the desired purity, is carried out in pressure swing adsorption (PSA) units that are operated at pressures reaching about 7 MPa using the Skarstrom cycle, involving multiple steps or stages; see the schematic in Figure 1. In the simplest case, the four steps in the sequence are as follows.[5−7]

(a) Pressurization (with the feed or raffinate product)
(b) High-pressure adsorption separation with the feed, with withdrawal of the purified raffinate product
(c) Depressurization, or "blowdown", countercurrent to the feed
(d) Desorption at the lower operating pressure. This is accomplished by evacuation or purging the bed with a portion of the purified raffinate product.

The use of layered beds, consisting of three different adsorbents, is an important characteristic of the currently employed PSA technology for $H_2$ purification.[2,8] In order to rationalize and understand the use of multilayer adsorbent beds, Figure 2a,b presents simulations of transient breakthroughs of 73/4/3/4/16 $H_2/N_2/CO/CH_4/CO_2$ mixture, typical of steam methane reformer off-gas,[3] in fixed bed adsorbers packed with

Received: May 13, 2020
Accepted: July 1, 2020
Published: July 10, 2020

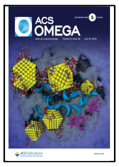

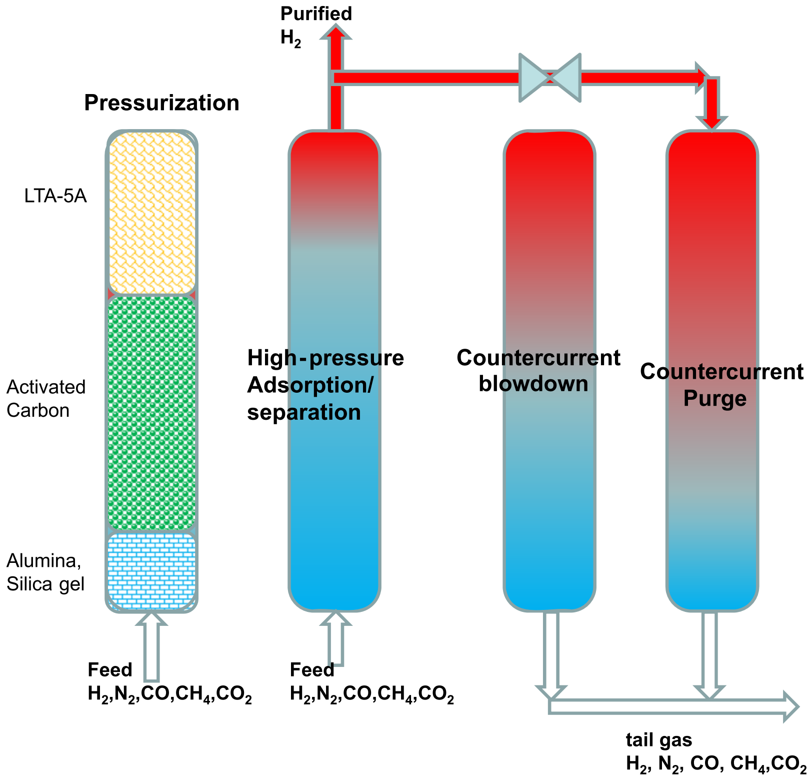

**Figure 1.** Sequential steps in the operation of a fixed bed adsorber in the Skarstrom cycle for $H_2$ purification.[2,5−7]

(a) AC and (b) LTA-5A zeolite[8−10] operating at 2 MPa total pressure and temperature $T$ = 313 K. Purified $H_2$ can be recovered during the time intervals between the breakthroughs of $H_2$ and $N_2$, as indicated by the arrows. The stronger binding of $N_2$ in LTA-5A, as compared to AC, is due to the contribution of the quadrupole moment of $N_2$ and its interaction with the charges of extraframework cations $Na^+$ and $Ca^{2+}$.[5,11] The quadrupole moment of $CO_2$ also leads to stronger binding in LTA-5A, causing significantly higher $CO_2$ capture capacity, as evidenced by the strongly delayed breakthrough of $CO_2$ with LTA-5A as compared to AC.[5,11] The strong binding of $CO_2$ in LTA-5A is disadvantageous because deep vacuum will be required to reduce the $CO_2$ loading to the desired level during the purge step (d) in Figure 1. Consequently, despite the superior separation performance of LTA-5A, resulting in higher productivity of pure $H_2$ per kilogram of adsorbent, LTA-5A is not used on its own in the currently used PSA schemes.[2,3] Commonly, the first layer is either alumina or silica that retains the water vapor. Then, an AC layer is used to selectively adsorb $CO_2$. The main task of the alumina and AC layers is to prevent the $H_2O$ vapor and $CO_2$ from reaching the zeolite layer.[2] The last layer is a cation-exchanged zeolite [such as LTA-5A, and NaX (=13X),[12] with $Na^+$ cations] with enhanced capacity for CO and $N_2$. For $H_2$ purification applications,[3,13−15] it is evident that $CO_2/H_2$ adsorption selectivity is not the "key" determinant of the achieved purity of $H_2$.

For $CO_2$ capture from flue gases from power plants, and from natural gas streams, MOFs offer energy-efficient alternatives to conventionally used amine absorption technologies.[16−21] In $CO_2$/flue gas and $CO_2$/natural gas separations, the process economics would demand high $CO_2$ capture capacity and concomitant ease of regeneration.[22]

For the production of alkene feedstocks of 99.95%+ purity required for polymerization reactors, cryogenic distillation columns, operated at high pressures and high reflux ratios, are commonly employed for large-scale separations of $C_2H_4/C_2H_6$ and $C_3H_6/C_3H_8$ mixtures. Many MOF developments have targeted alkene/alkane separations with the objective of eventually supplanting the energy-intensive distillation technologies.[23−29] Process economics would also demand high alkene productivities per kilogram adsorbent.

In steam cracking of ethane to produce ethene ($C_2H_4$), one of the byproducts is ethyne ($C_2H_2$). Typically, the $C_2H_2$ content of $C_2H_2/C_2H_4$ feed mixtures is 1%. Ethyne has a deleterious effect on the polymer products of ethene, such as polyethene. The impurity level of $C_2H_2$ in the $C_2H_4$ feed streams should be below 40 ppm in order to prevent the poisoning of catalysts used in the polymerization of $C_2H_4$. MOFs offer potential improvements to absorption technologies using dimethyl formamide as a solvent.[23,30−37] For 1/99 $C_2H_2/C_2H_4$ mixture separations, we would require that the MOF would have high productivity of pure alkene (<40 ppm $C_2H_2$) per kilogram of adsorbent.

Ethyne ($C_2H_2$) is an important building block in industrial chemical synthesis and is also widely used as a fuel in welding equipment. $C_2H_2$ is commonly manufactured by the partial combustion of $CH_4$ or comes from cracking of hydrocarbons. In the reactor product, $C_2H_2$ coexists with $CO_2$ or $C_2H_4$. Because of the similarity of molecular sizes and shapes ($C_2H_2$: 3.32 × 3.34 × 5.7 Å$^3$ and $CO_2$: 3.18 × 3.33 × 5.36 Å$^3$), the separation of $C_2H_2/CO_2$ mixtures is particularly challenging.[38,39] Because the boiling points of $C_2H_2$ (189.3 K) and $CO_2$ (194.7 K) are close, distillation separations need to operate at cryogenic temperatures and high pressures. A number of recently developed MOFs offer the potential of use in adsorptive separations of $C_2H_2/CO_2$ mixtures.[40−53]

The selective capture of $CO_2$ from the reactor effluents from the process for oxidative coupling of methane essentially requires for $CO_2$-selective separation of $CO_2/CH_4/C_2H_4/$

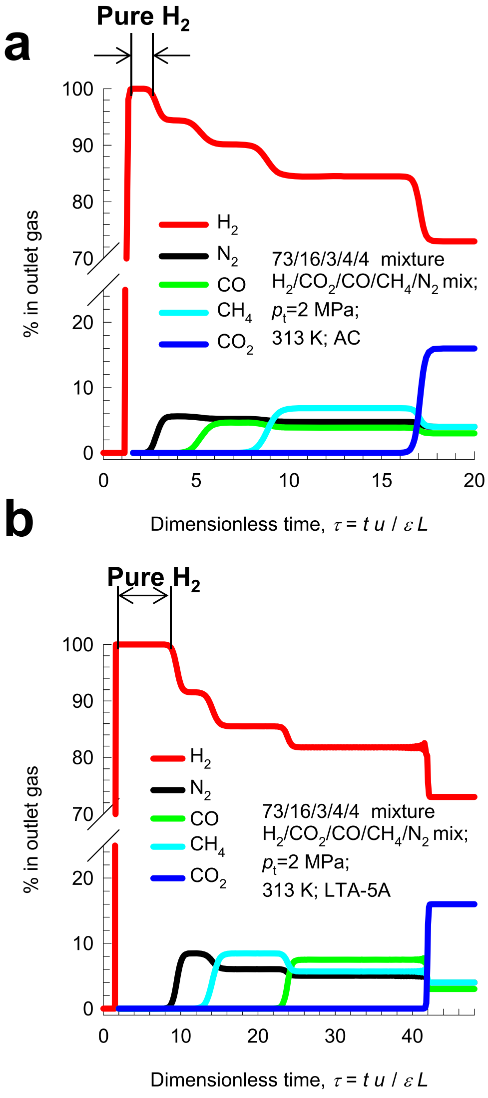

**Figure 2.** Transient breakthrough of 73/4/3/4/16 $H_2/N_2/CO/CH_4/CO_2$ mixtures in a fixed bed adsorber packed with (a) AC and (b) LTA-5A zeolite operating at a total pressure of 2 MPa and $T$ = 313 K. For presenting the breakthrough simulation results, we use as $x$-axis the dimensionless time, $\tau = tv/L$, where $L$ is the length of the adsorber and $v$ is the interstitial gas velocity.[63,122] Further information on input data and simulation details are provided in the Supporting Information.

$C_2H_6$ mixtures; the number of candidate adsorbent materials is surprisingly limited.[54−56]

Noble gases such as He, Ne, Ar, Kr, and Xe find a variety of applications.[57] For example, heliox (a mixture of He and $O_2$) is used for patients with respiratory difficulties and in deep-sea diving,[58] Ne is used in the familiar "neon sign" for advertisements. Kr and Xe are used in flash bulbs and lasers. Ar is used in filament bulbs and in electric arc welding as a shielding gas. Based on the differences in the boiling points, Ne (27 K), Ar (87 K), Kr (120 K), and Xe (165 K) are commercially produced by liquefaction of air, followed by cryogenic distillation. Alternatively, adsorptive separations, relying essentially on the differences in polarizabilities (cf. Figure 3), are realizable with a number of MOFs.[57,59,60]

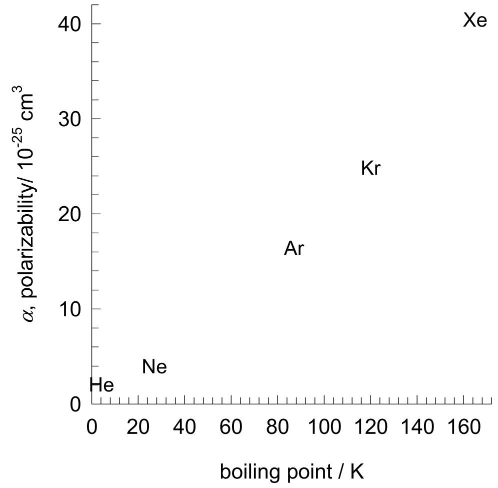

**Figure 3.** Boiling points and polarizabilities of noble gases culled from web sources.

The process demands in each of the aforementioned examples of mixture separations are different. The primary objective of this article is to provide a comparative assessment of the variety of metrics that are appropriate for screening and ranking candidate MOFs that are appropriate for the specific separation task in hand. The Supporting Information provides detailed structural information on the MOFs investigated, along with a detailed description of the methodology used for transient breakthrough simulations. For each of the chosen mixtures, the comparisons of the separation performance of various MOFs are on the basis of experimental data on the unary isotherms from published sources; the data sources are provided in the Supporting Information.

## 2. ADSORPTION SELECTIVITIES, UPTAKE CAPACITIES, AND TRANSIENT BREAKTHROUGHS

**2.1. Xe/Kr Separations.** To develop an understanding of the various metrics that determine the effectiveness of separations, let us consider the separation of 20/80 Xe(1)/Kr(2) mixtures in a fixed bed packed with CoFormate (=$Co_3(HCOO)_6$); the objective is to produce Kr with less

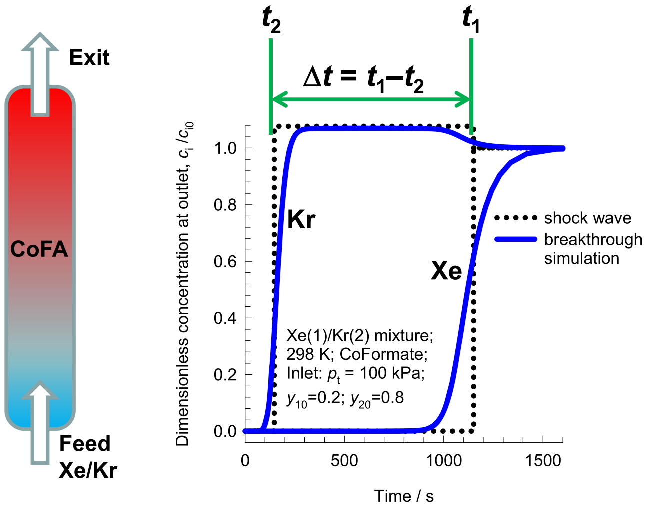

**Figure 4.** Transient breakthrough simulations (indicated by the solid blue line) for separation of 20/80 Xe/Kr mixtures at 298 K and 100 kPa in a fixed bed packed with CoFormate; these simulations include intracrystalline diffusion limitations. The dotted lines represent the shock wave model approximation.[63] The input data and calculation details are available in earlier works.[57,63,121]

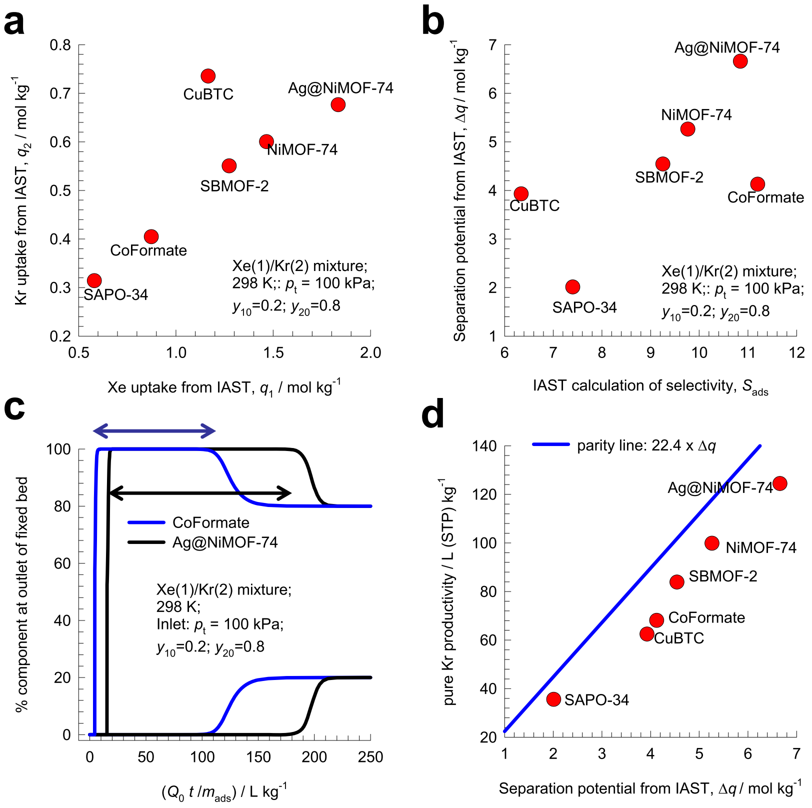

**Figure 5.** IAST calculations of (a) component loadings $q_2$ vs $q_1$ and (b) separation potential $\Delta q = q_1\frac{y_{20}}{y_{10}} - q_2$ vs adsorption selectivity $S_{ads}$ for 20/80 Xe(1)/Kr(2) mixture adsorption at 298 K and 100 kPa in six different MOFs: NiMOF-74[65,66] Ag@NiMOF-74,[66] CuBTC,[65,67] SBMOF-2,[59] CoFormate[61] (=$Co_3(HCOO)_6$), and SAPO-34.[60] (c) Comparison of the transient breakthrough simulations for separation of 20/80 Xe/Kr mixtures at 298 K and 100 kPa in fixed beds packed with CoFormate and Ag@NiMOF-74. The dimensionless concentrations at the exit of the fixed bed are plotted as a function of $Q_0t/m_{ads}$, where $Q_0$ is the volumetric flow rate of the gas mixture at the inlet to the fixed bed, expressed in L s$^{-1}$, at STP conditions. (d) Plot of the productivity of pure Kr, determined from breakthrough simulations, vs the IAST calculations of $\Delta q = q_1\frac{y_{20}}{y_{10}} - q_2$ for six different MOFs with $y_{10} = 0.2$; $y_{20} = 0.8$. Further information on input data and simulation details are provided in earlier works.[57,63,121]

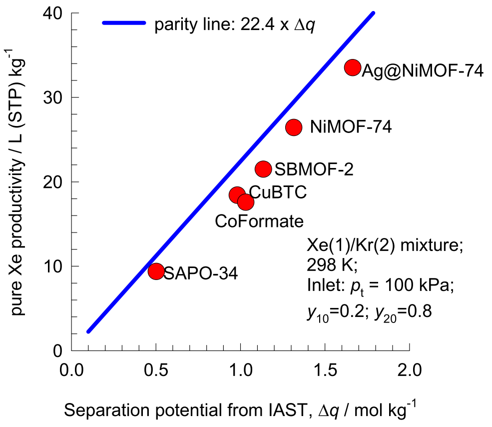

**Figure 6.** Plot of the productivity of pure Xe determined from transient desorption simulations for 20/80 Xe(1)/Kr(2) mixtures vs the IAST calculations of separation potential $\Delta q = q_1 - q_2\frac{y_{10}}{y_{20}}$ for six different MOFs with $y_{10} = 0.2$; $y_{20} = 0.8$. Further information on input data and simulation details are provided in earlier works.[57,63,121]

than say 1000 ppm Xe. Because of the commensurate positioning of Xe within its cages, CoFormate displays high Xe/Kr selectivity.[61] The continuous solid lines in Figure 4 represent transient breakthrough simulation results for the dimensionless concentrations $c_i/c_{i0}$ at the exit of the fixed bed.

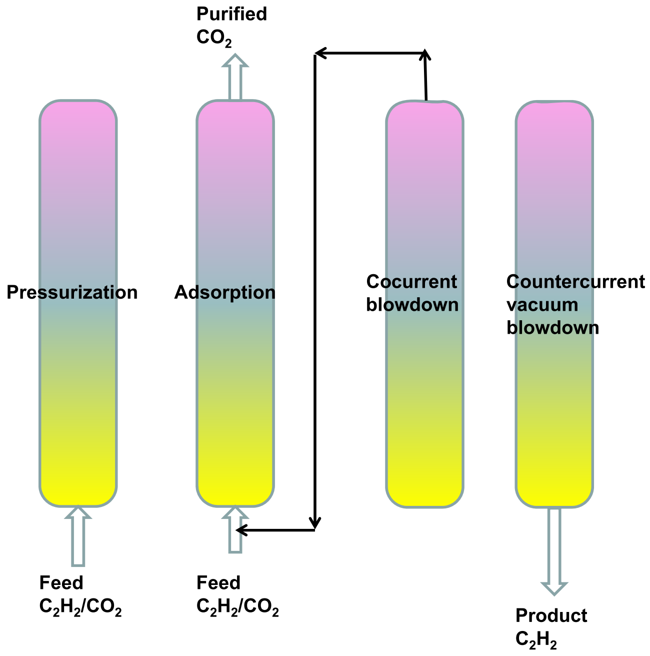

**Figure 7.** Sequential steps in the operation of a fixed bed adsorber in the Skarstrom cycle for $C_2H_2(1)/CO_2(2)$ separation.

https://dx.doi.org/10.1021/acsomega.0c02218
ACS Omega 2020, 5, 16987−17004

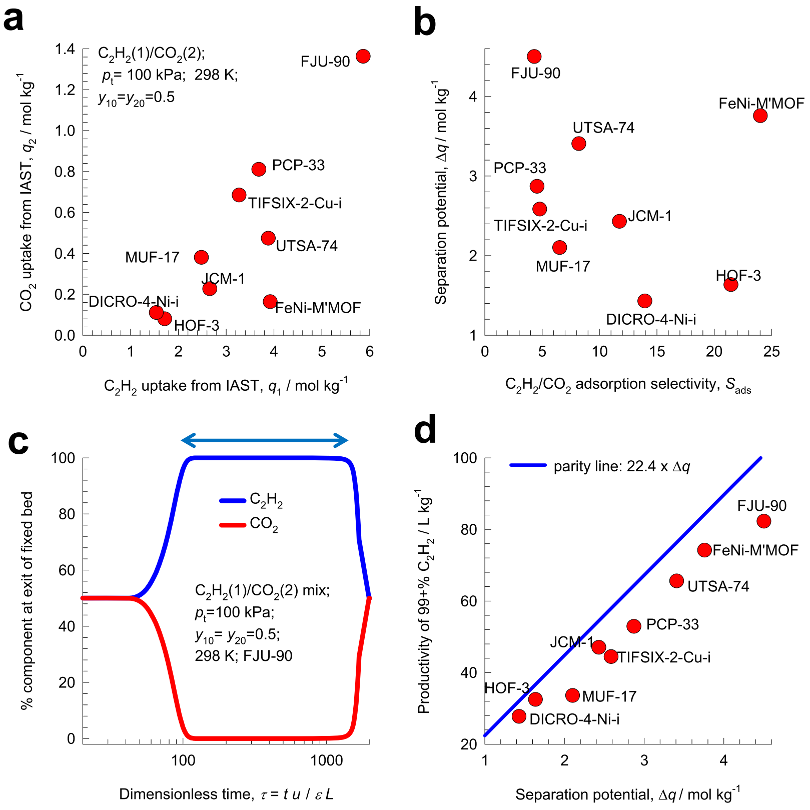

**Figure 8.** IAST calculations of (a) component loadings $q_2$ vs $q_1$ and (b) separation potential $\Delta q = q_1 - q_2\frac{y_{10}}{y_{20}}$ vs adsorption selectivity $S_{ads}$ for the adsorption of $C_2H_2(1)/CO_2(2)$ mixtures in nine different MOFs operating at 298 K and 100 kPa. (c) Simulations of transient desorption (blowdown) under deep vacuum (0.2 Pa total pressure and 298 K). During the time interval indicated by the arrow, the $C_2H_2$ product containing <1% $CO_2$ can be recovered. (d) Productivity of 99%+ pure $C_2H_2$ product determined by transient desorption simulations for PCP-33, HOF-3, TIFSIX-2-Cu-i, JCM-1, DICRO-4-Cu-i, MUF-17, UTSA-74, FJU-90, and FeNi-M′MOF at 298 K and 100 kPa, plotted as a function of the separation potential $\Delta q = q_1 - q_2\frac{y_{10}}{y_{20}}$ with $y_{10} = y_{20} = 0.5$. Further information on input data and simulation details are provided in earlier works.[41,43,63,121]

The breakthroughs have distended characteristics that are caused by intracrystalline diffusional limitations. For subsequent discussions, it is useful to also consider the limiting scenario in which the concentration fronts traverse the fixed bed in the form of shock waves;[62,63] the shock wave model approximation is shown by the dotted lines in Figure 4; further details of the shock wave model are provided in the Supporting Information. Because the shock wave model has sharp fronts, the separation performance is the maximum achievable, and this simplified model helps to derive simple expressions for the metrics that describe the performance of fixed bed adsorbers.

In the shock wave model, the traversal velocity for the more strongly adsorbed Xe is significantly lower than that of the poorly adsorbed Kr.[6,7] The Xe capture capacity of CoFormate, $q_1$, expressed as moles captured per kilogram of adsorbent in the fixed bed can be calculated from a material balance

$$q_1 = \frac{y_{10}c_tQ_0}{m_{ads}}t_1 \tag{1}$$

In eq 1, $y_{10}$ is the mole fraction of Xe at the inlet to the bed, $Q_0$ is the volumetric flow of the feed gas mixture with total molar concentration, $c_t = p_t/RT$, $t_1$ is the breakthrough time for Xe, and $m_{ads}$ is the mass of the adsorbent. We define the displacement time interval $\Delta t = t_1 - t_2$ as the difference between the breakthrough times of Xe(1) and Kr(2); during this interval, pure Kr can be recovered. The productivity of purified Kr, $\Delta q$, that is collected during the displacement interval can be determined from the shock wave model[63]

$$\Delta q = \frac{c_tQ_0}{m_{ads}}\Delta t = q_1\frac{y_{20}}{y_{10}} - q_2 \tag{2}$$

where $q_2$ is the uptake of Kr in the bed

$$q_2 = \frac{y_{20}c_tQ_0}{m_{ads}}t_1 - \Delta q \tag{3}$$

Because its derivation is based on the idealized shock wave model, the quantity $\Delta q$, dubbed the separation potential, represents the maximum productivity of the less strongly adsorbed component that can be recovered.

The adsorption selectivity, $S_{ads}$, defined by

$$S_{ads} = \frac{q_1/q_2}{y_{10}/y_{20}} \tag{4}$$

can be related to the breakthrough times by combining eqs 1−4

$$S_{ads} = \frac{1}{1 - \frac{\Delta t}{y_{20}t_1}}; \qquad \frac{\Delta t}{t_1} = \frac{\Delta q}{q_1/y_{10}} = y_{20}\left(1 - \frac{1}{S_{ads}}\right) \tag{5}$$

Increasing values of adsorption selectivities, $S_{ads}$, results in an increase in the values of $\Delta t/t_1$ and $\frac{\Delta q}{q_1/y_{10}}$. This implies that as the

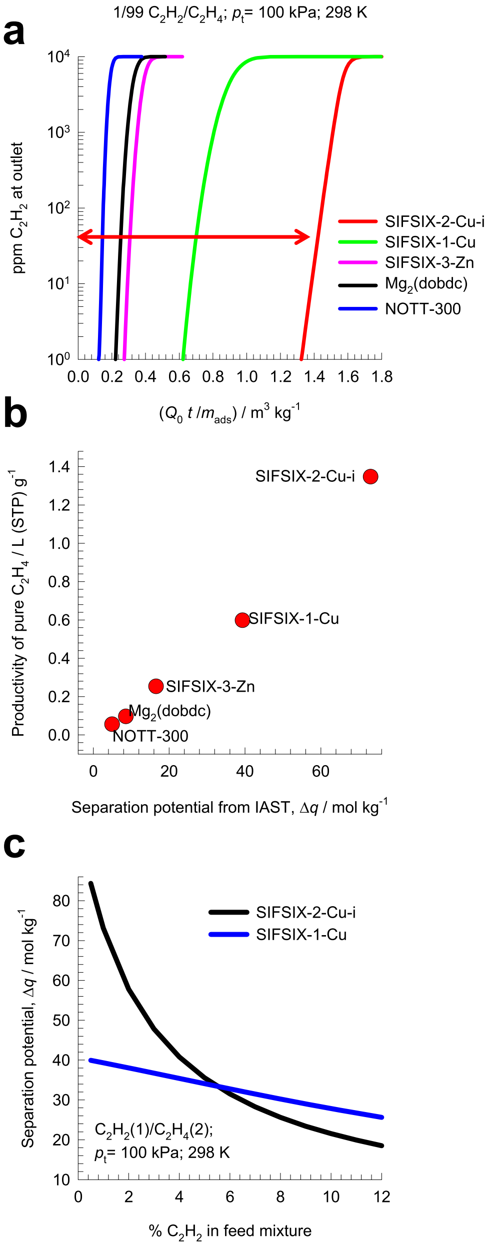

**Figure 9.** (a) Transient breakthrough simulations for 1/99 $C_2H_2/C_2H_4$ mixture adsorption at 298 K and 100 kPa in a fixed bed packed with five different MOFs. The ppm $C_2H_2$ in the gas mixture at the outlet of the fixed bed is plotted as a function of $Q_0t/m_{ads}$, where $Q_0$ is the volumetric flow rate of the gas mixture at the inlet to the fixed bed, expressed in $m^3\ s^{-1}$, at STP conditions. (b) Productivity of pure $C_2H_4$, containing less than 40 ppm $C_2H_2$, plotted as a function of the separation potential $\Delta q = q_1\frac{y_{20}}{y_{10}} - q_2$ determined from IAST with $y_{10} = 0.01$; $y_{20} = 0.99$. (c) Separation potential, $\Delta q$, of SIFSIX-2-Cu-i and SIFSIX-1-Cu, plotted as a function of the % $C_2H_2$ in the feed mixture. Further information on input data and simulation details are provided in the Supporting Information.

selectivity increases, the breakthrough of Kr occurs increasingly earlier

$$S_{ads} \to \infty; \qquad t_2 \to 0; \qquad \Delta t \to y_{20} t_1 \tag{6}$$

Although a high value of $S_{ads}$ is always a desirable characteristic, this metric does not guarantee a high productivity of pure Kr that is required of the "best" MOF. The highest productivity of Kr will be offered by the MOF that has the highest value of separation potential $\Delta q = q_1y_{20}/y_{10} - q_2$, which should be regarded as a combined selectivity−capacity metric.[63] In order to underscore this observation, Figure 5a,b presents the ideal adsorbed solution theory[64] (IAST) calculations of (a) component loadings $q_2$ versus $q_1$ and (b) separation potential $\Delta q = q_1\frac{y_{20}}{y_{10}} - q_2$ versus adsorption selectivity $S_{ads}$ for adsorption of 20/80 Xe(1)/Kr(2) mixtures in NiMOF-74,[65,66] Ag@NiMOF-74,[66] CuBTC,[65,67] SBMOF-2,[59] CoFormate,[61] and SAPO-34.[60] The MOF with the highest value of $S_{ads}$ is CoFormate; however, the highest $\Delta q$ is achieved by Ag@NiMOF-74. The presence of well-dispersed Ag nanoparticles in Ag@NiMOF-74 causes stronger van der Waals interactions of the polarizable Xe atoms; this results in the higher uptakes and the highest $\Delta q$.

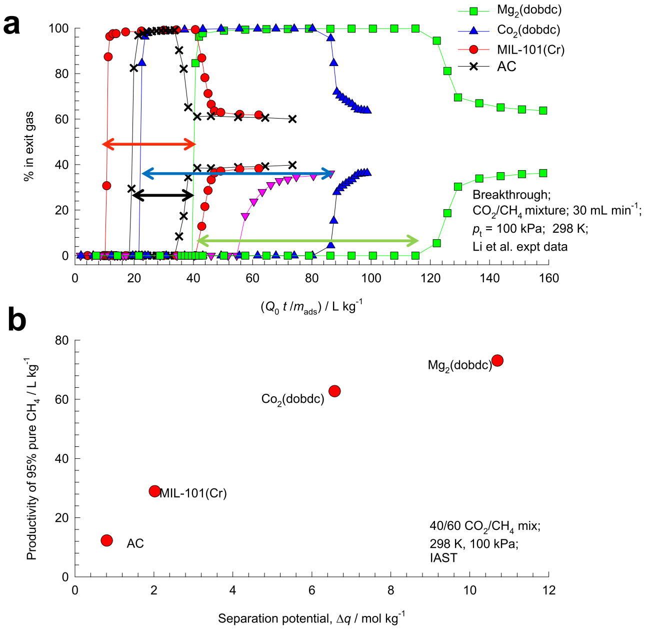

**Figure 10.** (a) Experimental breakthroughs for $CO_2/CH_4$ mixtures in a packed bed with $Mg_2$(dobdc), $Co_2$(dobdc), MIL-100(Cr), and AC at 298 K. The partial pressures at the inlet are $p_1 = 40$ kPa, $p_2 = 60$ kPa, and $p_t = 100$ kPa. The experimental data, indicated by the symbols, are from Li et al.[68] The % $CO_2$ and % $CH_4$ in the exit gas phase are plotted as a function of $Q_0t/m_{ads}$. (b) Productivity of 95% pure $CH_4$ plotted as a function of separation potential.

Because the productivity of pure Kr, $\Delta q$, is proportional to the displacement time interval, $\Delta t = t_1 - t_2$, an alternative procedure for screening MOFs for Xe/Kr separations would be on the basis of the displacement intervals, determined by comparing transient breakthroughs in fixed beds, that are determined from experimental data or transient breakthrough simulations. Figure 5c compares the transient breakthrough simulations for Ag@NiMOF-74 and CoFormate on this basis. The transient breakthrough simulation methodology is described in detail in the Supporting Information. Briefly, the assumptions made in the simulations are as follows: (1) axial dispersion effects are considered to be negligible, (2) the mixture adsorption equilibrium can be described using IAST, (3) the column pressure drop is of negligible importance, and (4) the total pressure remains constant during the operation. Because the breakthrough times are dependent on the mass of the adsorbent, $m_{ads}$, and the volumetric flow rate, $Q_0$, the appropriate comparison of transient breakthroughs for different MOFs is

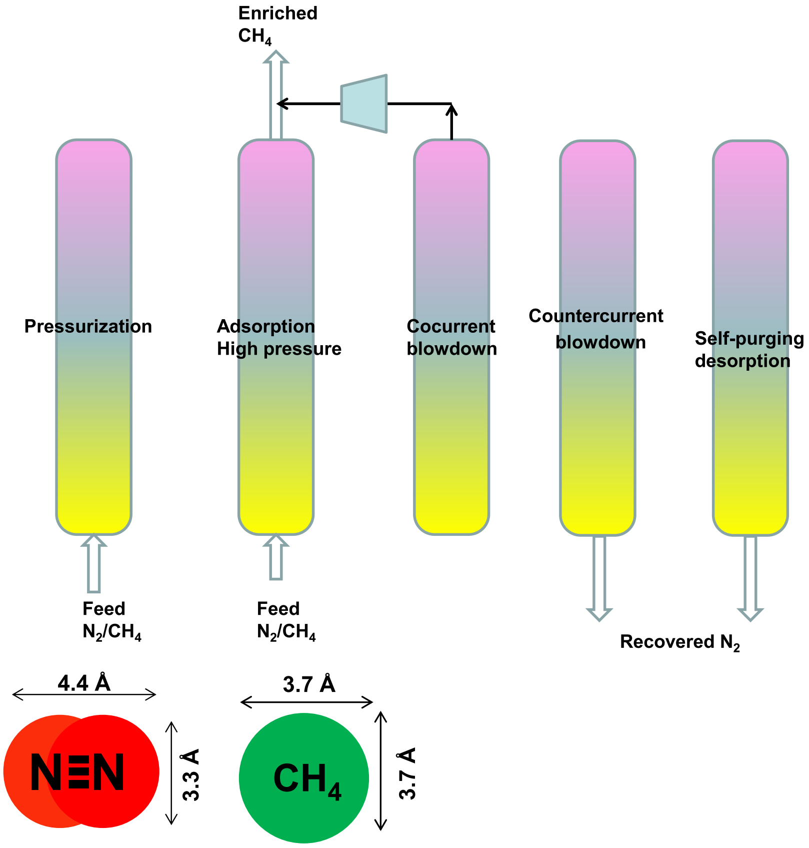

**Figure 11.** Different steps in the production of purified $CH_4$ using an adsorbent such as LTA-4A zeolite, Ba-ETS-4, and clinoptilolites, which rely on kinetic selectivity. The scheme shows the sequence of processing of a single bed in a multibed PSA scheme. Adapted from Bhadra and Farooq[70] and Jayaraman et al.[72]

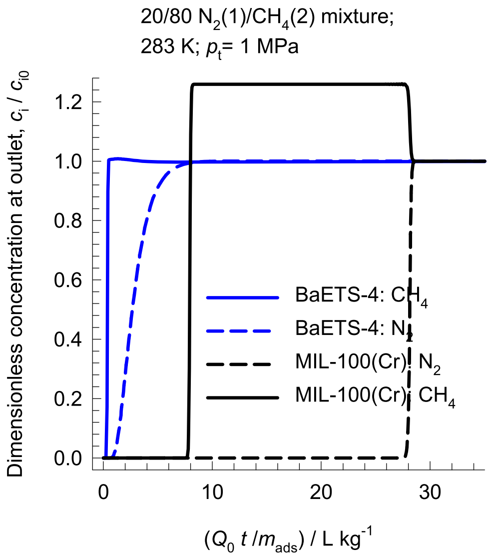

**Figure 12.** Comparison of the transient breakthroughs of 20/80 $N_2(1)/CH_4(2)$ mixtures in a fixed bed adsorber packed with MIL-100(Cr) and Ba-ETS-4 operating at 283 K and total pressure $p_t$ = 1 MPa. Further information on input data and simulation details are provided in the Supporting Information.

to use the parameter $Q_0t/m_{ads}$ as the $x$-axis in place of time; indeed, this parameter may be viewed as a "corrected" time. It is also a common practice to use the value of $Q_0$ at STP conditions. Noteworthily, the breakthroughs of both Ag@NiMOF-74 and CoFormate have distended characteristics. Because of intracrystalline diffusion limitations, the breakthrough characteristics of CoFormate are more distended than that of Ag@NiMOF-74. In the industry, the process requirement would demand the production of Kr containing <1000 ppm Xe. During the displacement intervals indicated by the arrows, the industrial process requirements may be met.[57] To determine the actual amount of Kr of desired purity that may be recovered, the total amount of Kr that exits the fixed bed during the displacement interval is determined by sampling of the exit gas from the fixed bed; from such sampling, the productivities of pure Kr are 125 L (STP) kg$^{-1}$ for Ag@NiMOF-74 and 68 L (STP) kg$^{-1}$ for CoFormate. Despite having the highest $S_{ads}$ value, the significantly poorer productivity of CoFormate is directly ascribable to its lower uptake capacity (cf. Figure 5a). Figure 5d plots the productivities of pure Kr from transient breakthroughs of six different MOFs as a function of the corresponding IAST calculations of $\Delta q$. The near-linear relation between the two sets confirms that IAST calculations of the separation potential $\Delta q$ may be used for screening purposes. Also shown by the continuous solid line in Figure 5d is the parity line 22.4 × $\Delta q$ for the productivities. Because of the distended nature of the transient breakthroughs in Figure 5c, the actual productivities are lower than 22.4 × $\Delta q$.

The MOF crystallites in the fixed bed at the end of the adsorption cycle are predominantly rich in the more strongly adsorbing Xe. Pure Xe can be recovered during the desorption cycle by the application of deep vacuum. The maximum productivity of pure Xe can also be derived from the use of the shock wave model[63]

https://dx.doi.org/10.1021/acsomega.0c02218
*ACS Omega* 2020, 5, 16987−17004

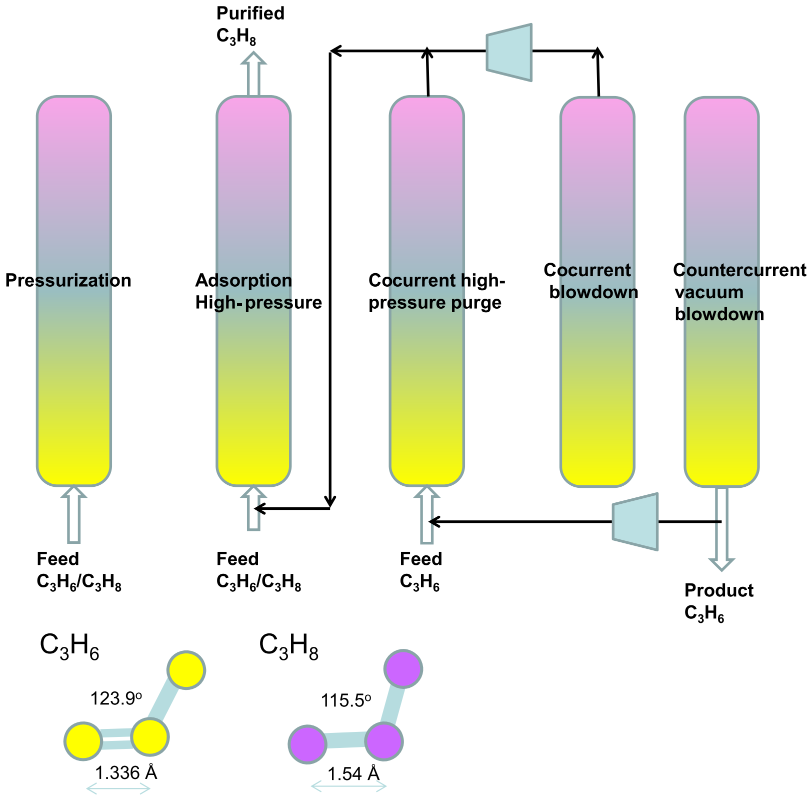

**Figure 13.** Five-step PSA process for separating $C_3H_6/C_3H_8$ mixtures.[77,78,81]

$$\Delta q = q_1 - q_2 \frac{y_{10}}{y_{20}}; \qquad \text{desorption cycle} \tag{7}$$

Figure 6 plots the productivities of pure Xe, containing <1000 ppm Kr, from transient desorption simulations using six different MOFs, against the corresponding IAST calculations of $\Delta q$, calculated using eq 7 with $y_{10} = 0.2$; $y_{20} = 0.8$. The relation between the actual productivities (symbols) and $\Delta q$ is not perfectly linear. For example, the Xe productivity of CoFormate is slightly lower than that of CuBTC, despite the fact that the separation potential $\Delta q$ of CoFormate is higher than that of CuBTC. IAST calculations of the separation potential $\Delta q$, from eq 7, for screening of MOFs will be of inadequate accuracy in cases of strong diffusional influences.

**2.2. $C_2H_2/CO_2$ Mixture Separations.** For separation of $C_2H_2(1)/CO_2(2)$ mixtures, most of the suggested MOFs such as PCP-33,[47] HOF-3,[48] TIFSIX-2-Cu-i,[49] JCM-1,[50] DICRO-4-Cu-i,[51] MUF-17,[52] UTSA-74,[46] FJU-90,[43] and FeNi-M′MOF[41] are selective to $C_2H_2$. Consequently, the desired ethyne product is available in the blowdown phase of the Skarstrom cycle of fixed bed operations, as shown in the schematic in Figure 7.

For the nine selected MOFs, Figure 8a,b presents the IAST calculations of (a) component loadings $q_2$ versus $q_1$ and (b) separation potential $\Delta q = q_1 - q_2 \frac{y_{10}}{y_{20}}$ versus adsorption selectivity $S_{ads}$. It is noteworthy that FJU-90 has the highest uptake capacity for ethyne, whereas the highest selectivity is afforded by FeNi-M′MOF. The separation performance in fixed bed adsorbers is dictated by a combination of selectivity and uptake capacities. Figure 8c presents the simulations of the vacuum blowdown cycle in which the equilibrated fixed bed of FJU-90 crystallites at the end of the adsorption cycle is subject to deep vacuum. During the time interval indicated by the arrow, $C_2H_2$ of the desired purity can be recovered from the gas mixture exiting the fixed bed. For a desired purity of 99%+, the amount of $C_2H_2$ that is recoverable can be determined from a material balance on the adsorber. These productivity values, expressed as *L* of the desired product (at STP) per kilogram of adsorbent in the packed bed, for the nine different MOFs are plotted in Figure 8d as the *y*-axis. The *x*-axis in Figure 8d is the separation potential, $\Delta q$, calculated using eq 7 with $y_{10} = y_{20} = 0.5$, which represents the maximum $C_2H_2$ productivity that is achievable if the concentration "fronts" traversed the column in the form of shock waves during the desorption cycle. We note that the productivities determined from the transient breakthrough simulations (denoted as symbols) are near linearly related to $\Delta q$. Also shown by the continuous solid line in Figure 8d is the parity line 22.4 × $\Delta q$ for the productivities. Because of the distended nature of the transient desorption breakthroughs, the actual productivities are lower than the parity values. The important conclusion to emerge is that separation potential, $\Delta q$, is the appropriate metric to use in the screening of MOFs for $C_2H_2/CO_2$ mixture separations. The MOF with the highest $C_2H_2$ productivity is FJU-90, which does not possess the highest selectivity but the highest $\Delta q$.

**2.3. $C_2H_2/C_2H_4$ Mixture Separations.** With great potential for separation of $C_2H_2/C_2H_4$ mixtures are a series of three-dimensional (3D) coordination networks composed of inorganic anions of $(SiF_6)^{2-}$ (hexafluorosilicate, SIFSIX).[30] The pore sizes within this family of SIFSIX materials can be systematically tuned by changing the length of the organic (=pyridine) linkers, the metal (=Cu, Ni, or Zn) node, and/or the framework interpenetration. Figure 9a compares the transient breakthroughs for 1/99 $C_2H_2(1)/C_2H_4(2)$ mixtures using SIFSIX-1-Cu, SIFSIX-2-Cu-i, SIFSIX-3-Zn, $Mg_2(dobdc)$, and NOTT-300; the ppm $C_2H_2$ in the gas mixture at the outlet of the

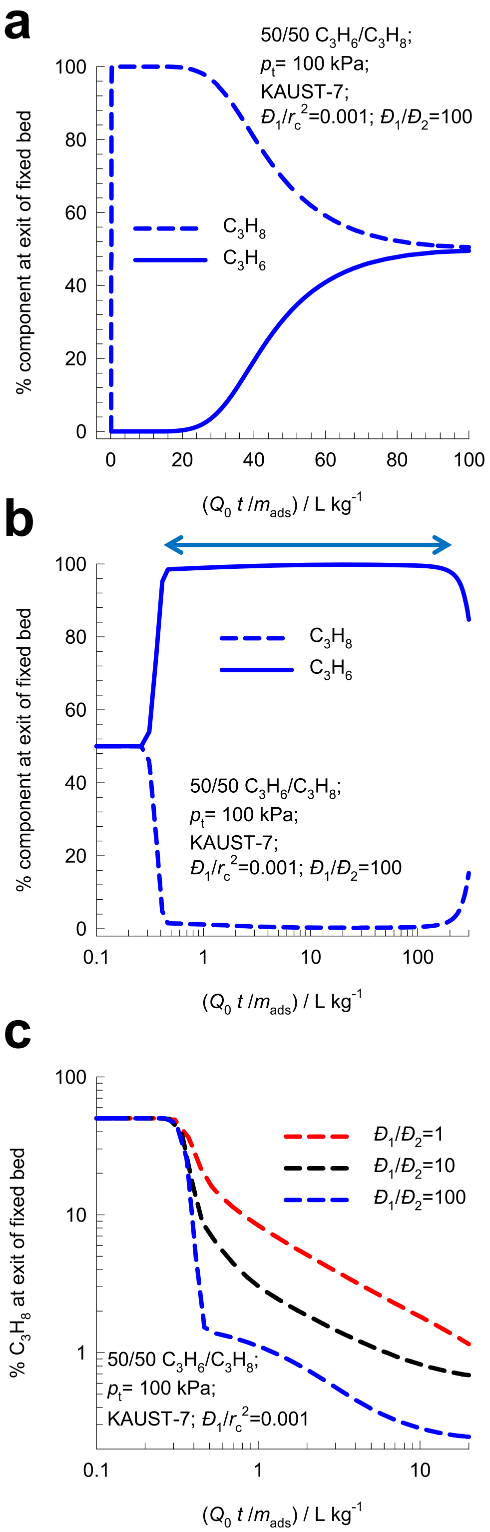

**Figure 14.** Transient breakthrough simulations for (a) adsorption and (b,c) desorption cycles for the separation of $C_3H_6/C_3H_8$ mixtures in a fixed bed adsorber packed with KAUST-7 operating at 298 K and 100 kPa; the feed compositions are $y_{10} = y_{20} = 0.5$. (c) Three different scenarios for the ratios of diffusivities $Đ_1/Đ_2 = 1$, 10, and 100 are compared, while maintaining $Đ_1/r_c^2 = 1 \times 10^{-3}$ s$^{-1}$. Further information on input data and simulation details are provided in the Supporting Information.

fixed bed is plotted as a function of $Q_0t/m_{ads}$, where $Q_0$ is the volumetric flow rate of the gas mixture at the inlet to the fixed bed at STP conditions. From a material balance on the adsorber, we can determine the productivity of purified $C_2H_4$, containing less than 40 ppm. The productivity of pure $C_2H_4$ is found to be a near-linear function of the separation potential $\Delta q$ determined from IAST; see Figure 9b. The highest productivity is obtained with SIFSIX-2-Cu-i (2 = 4,4′-dipyridylacetylene and i = interpenetrated);[30] in this case, each $C_2H_2$ molecule is bound by two F atoms from different nets. The binding of $C_2H_4$ with the F atoms is weaker because it is far less acidic than $C_2H_2$. This confirms that the separation potential $\Delta q$ is the appropriate metric for screening MOFs for $C_2H_2/C_2H_4$ mixture separations.

Figure 9c compares the separation potentials of SIFSIX-2-Cu-i and SIFSIX-1-Cu as a function of the % $C_2H_2$ in the feed mixture. While the interpenetrated SIFSIX-2-Cu-i has the superior performance for feed compositions below 5% $C_2H_2$, SIFSIX-1-Cu, with a more open structure, has the better separation capability at higher % $C_2H_2$ in feed; this trend is verified in the experiments reported by Cui et al.[30]

### 2.4. $CO_2$ Capture from Natural Gas.

For $CO_2$ capture from natural gas streams, the process economics would demand the high capture capacity, concomitant with high productivity of pure $CH_4$. Li et al.[68] report on the experimental results of transient breakthroughs for 40/60 $CO_2(1)/CH_4(2)$ mixtures in a packed bed with $Mg_2$(dobdc), $Co_2$(dobdc), MIL-100(Cr), and AC at 298 K temperature and 100 kPa total pressure. The masses of the adsorbents in the packed tube are not the same for each MOF, and therefore, their experimental data have been replotted in Figure 10a using $Q_0t/m_{ads}$ as the $x$-axis. For each of the five materials, there is a displacement interval (indicated by the arrows) during which purified $CH_4$ can be recovered. The $CH_4$ productivities follow the hierarchy $Mg_2$(dobdc) > $Co_2$(dobdc) > MIL-100(Cr) > AC. Figure 10b presents a plot of productivity of 95%+ pure $CH_4$ as a function of the separation potential $\Delta q = q_1y_{20}/y_{10} - q_2$. The 95%+ pure $CH_4$ productivities follow the same hierarchy as the $\Delta q$ values, indicating that the separation potential can be used for screening purposes.

### 2.5. $N_2/CH_4$ Mixture Separations.

Although natural gas reserves may contain $N_2$ in concentrations ranging to about 20%,[69] the nitrogen content must be reduced to below 4% in order to meet pipeline specifications.[70] For large capacity wells, it is most economical to employ cryogenic distillation for nitrogen removal. However, for smaller natural gas reserves, PSA separations become more cost-effective, especially because the feed mixtures are available at high pressures.[69,70] The adsorbent materials in the PSA units need to be selective to $N_2$, which is present in smaller concentrations than $CH_4$. For most known adsorbents, the adsorption selectivity for separation of $N_2/CH_4$ mixtures is in favor of $CH_4$ because of its higher polarizability.

One practical solution is to rely on diffusion selectivities by using microporous materials, such as LTA-4A zeolite, ETS-4 (ETS = Engelhard Titano-Silicate; ETS-4 is also named as CTS-1 = Contracted Titano Silicate-1), and clinoptilolites, which have significantly higher diffusivities of $N_2$ compared to that of $CH_4$.[5,70−73] The "spherical" $CH_4$ (3.7 Å) is much more severely constrained inside the narrow pores of such materials, whereas the "pencil-like" nitrogen molecule (4.4 Å × 3.3 Å) hops lengthwise with higher diffusivity. By tuning the size of the microporous channels of cation-exchanged ETS-4, such as Ba-ETS-4, $CH_4$ can be practically excluded from the pores.

Bhadra[70,74] have developed a detailed mathematical model for a PSA scheme for purification of natural gas using Ba-ETS-4, using the steps shown in Figure 11. In this scheme, the inclusion

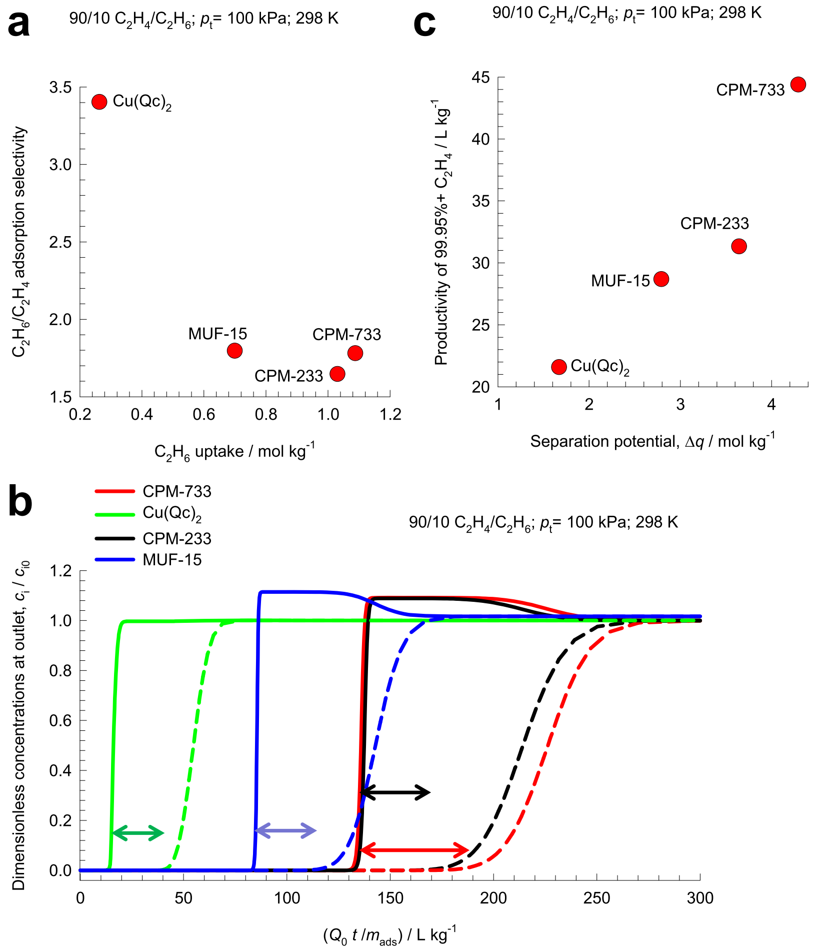

**Figure 15.** (a) IAST calculations of the $C_2H_6$ uptake $q_2$ vs the separation selectivity $S_{ads}$ of 90/10 $C_2H_4/C_2H_6$ mixture adsorption at 298 K and 100 kPa in four different MOFs. (b) Transient breakthrough simulations for the separation of 90/10 $C_2H_4/C_2H_6$ mixture adsorption at 298 K and 100 kPa in fixed beds packed with Cu(Qc)$_2$, MUF-15, CPM-233, and CPM-733. (c) Productivity of 99.95%+ pure $C_2H_4$ product recovered during the displacement intervals, plotted as function of the separation potential $\Delta q$. Further information on input data and simulation details are provided in the Supporting Information.

of the cocurrent blowdown step (suggested by Jayaraman et al.[72] for $N_2/CH_4$ mixture separations with clinoptilolites) increases the $CH_4$ recovery. At the end of the countercurrent blowdown step, the bed contains both nitrogen (fast diffusing) and methane (slow diffusing). Thus, if the bed is simply closed at one end and left for a period of time, the nitrogen will diffuse out first, followed by methane, so the system is, in effect, self-purging (fifth step in the sequence).

In a recent article, Yoon et al.[75] have reported that MIL-100(Cr), activated at 523 K, shows adsorption selectivity in favor of $N_2$. However, an important disadvantage of this material for use in natural gas purification is that $CH_4$ is not completely excluded. Figure 12 compares the transient breakthrough of 20/80 $N_2(1)/CH_4(2)$ mixtures in a fixed bed adsorber packed with MIL-100(Cr) and Ba-ETS-4, operating at 283 K and total pressure $p_t$ = 1 MPa. We note that the breakthrough of $CH_4$ occurs significantly later than that with BaETS-4, implying that a significant amount of $CH_4$ gets adsorbed. Consequently, even after cocurrent blowdown, a significant proportion of $CH_4$ will remain in the void spaces of the fixed bed packed with MIL-100(Cr) and will be "lost" along with $N_2$ in the final blowdown step; this implies that recovery of 96%+ pure $CH_4$ is likely to be unacceptably low with MIL-100(Cr). Candidate adsorbents for $N_2/CH_4$ separations must disallow the ingress of $CH_4$ inside the pores.

### 2.6. Separation of $C_2H_4/C_2H_6$ and $C_3H_6/C_3H_8$ Mixtures.

Both ethene ($C_2H_4$) and propene ($C_3H_6$) are important precursors for the manufacture of a variety of polymers. Propene is a byproduct from the steam cracking of liquid feedstocks such as naphtha and liquefied petroleum gas, as well as off-gases produced in fluid catalytic cracking units in refineries. The key processing steps for preparing feedstocks for polymer production are the separations of $C_2H_4/C_2H_6$ and $C_3H_6/C_3H_8$ mixtures, which are traditionally carried out in distillation columns. Because of small differences in the boiling points, the relative volatilities of $C_2H_4/C_2H_6$ and $C_3H_6/C_3H_8$ separations are in the range 1.1−1.2. In order to satisfy the 99.95%+ purity requirement of alkene feedstocks to polymerization reactors, the distillation columns are tall (150−200 trays) and operate at cryogenic temperatures, high pressures, and high reflux ratios (≈15). Use of adsorptive separations may result in reduced energy consumption.

Each of the unsaturated alkenes $C_2H_4$ and $C_3H_6$ possesses a $\pi$-bond, and the preferential adsorption of alkene from the corresponding alkane with the same number of C atoms can be achieved by choosing zeolitic adsorbents with extraframework cations [e.g., LTA-4A zeolite[76,77] and NaX (=13X) zeolite[76,78]]

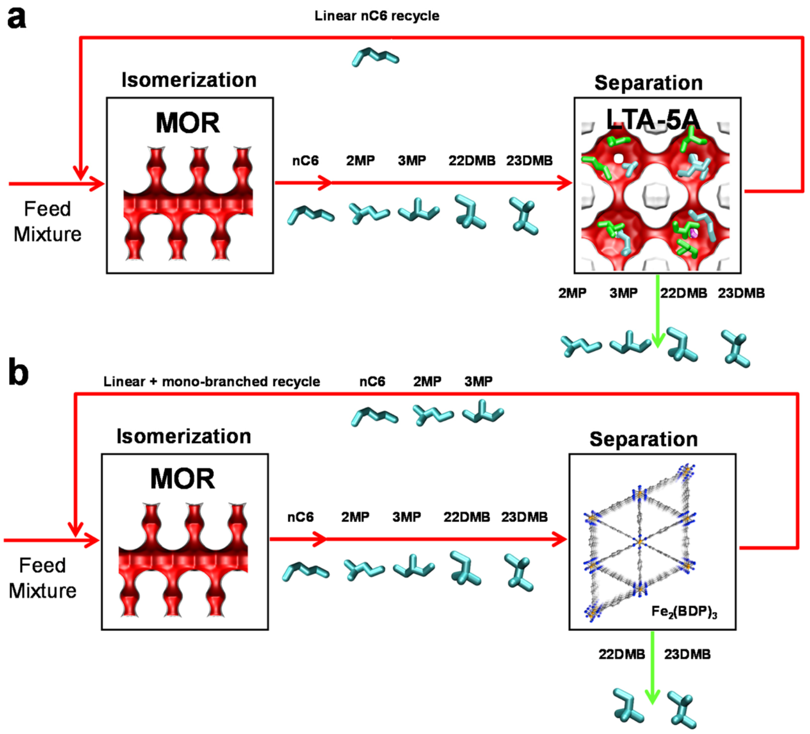

**Figure 16.** (a) Currently employed processing scheme for *n*C6 isomerization and a subsequent separation step using LTA-5A zeolite. (b) Improved processing scheme for the *n*C6 isomerization process. Further process background details are provided in the Supporting Information.

or MOFs with unsaturated "open" metal sites[23,79] (e.g., $M_2$(dobdc)[23,79] [M = Mg, Mn, Co, Ni, Zn, and Fe; dobdc$^{4-}$ = 2,5-dioxido-1,4-benzenedicarboxylate] and CuBTC[80]). All of the atoms of $C_2H_4$ lie on the same plane, and its dipole moment is zero; however, it does possess a quadrupole moment. It is to be noted that the polarizability of the alkane ($C_2H_6$, $C_3H_8$) is slightly higher than that of the corresponding alkene ($C_2H_4$ and $C_3H_6$).

An important disadvantage of the alkene/alkane separations with the adsorbents listed above is that the desired alkene product, required for the production of polymer-grade feedstock, can only be recovered in the desorption phase. In practice, it becomes necessary to operate with multiple beds involving five different steps, as schematized in Figure 13; the $C_3H_6$ product of the desired purity is recovered in the final step by countercurrent vacuum blowdown.[77,78,81] The recovery of high-purity $C_3H_6$ product in the final vacuum blowdown step is expected to be enhanced if $C_3H_8$ is (almost) excluded during the high-pressure adsorption cycle. Near-total exclusion of $C_3H_8$ is achievable by kinetically based separations using cage-type zeolites with eight-ring windows such as CHA and LTA-4A zeolites.[81,82] An alternative is to employ a customized MOF such as NbOFFIVE-1-Ni (=KAUST-7) with pyrazine as the organic linker.[24] The use of bulkier $(NbOF_5)^{2-}$ pillars causes tilting of the pyrazine molecule on the linker, resulting in an effective aperture of 0.30 nm. This reduced aperture permits ingress of the smaller $C_3H_6$ molecules but practically excludes $C_3H_8$, relying on subtle differences in bond lengths and bond angles.

Figure 14a,b presents the simulations of the transient breakthroughs for the (a) adsorption and (b) desorption cycles for separation of equimolar $C_3H_6(1)/C_3H_8(2)$ mixtures in a fixed bed adsorber packed with KAUST-7 operating at 298 K and 100 kPa. During the time interval indicated by the arrow in Figure 14b, the $C_3H_6$ product of desired purity can be recovered. Because of the significantly lower diffusivity of $C_3H_8$, the desorption process is self-purging.[7,83] In the last step shown in Figure 13, if the bed is simply closed at the one end and left for a period of time, $C_3H_6$ will diffuse out first, followed by $C_3H_8$. Figure 14c presents a comparison of the transient desorption using three different ratios of intracrystalline diffusivities $Đ_1/Đ_2$ = 1, 10, and 100. From a material balance on the adsorber, the productivities of 99%+ pure $C_3H_6$ can be determined; the values are, respectively, 15.7, 18.9, and 24.3 L kg$^{-1}$ at STP for the three scenarios. Because of the sensitivity of the $C_3H_6$ productivity to the values of intracrystalline diffusivities, a detailed process design exercise, such as that reported by Khalighi et al.,[81,82] will be required in order to compare the $C_3H_6$ productivities of KAUST-7, with other MOFs; simple IAST calculations of $\Delta q$ and $S_{ads}$ are unlikely to be sufficiently accurate for reliable screening.

For $C_2H_4/C_2H_6$ separations, near-total exclusion of $C_2H_6$ is achieved by use of ultramicroporous MOF $[Ca(C_4O_4)(H_2O)]$ that possesses rigid one-dimensional (1D) channels.[25] The 1D channels are of similar size to $C_2H_4$ molecules (all atoms of which lie on the same plane), but owing to the size, shape, and rigidity of the pores, they practically exclude $C_2H_6$.

For $C_2H_4/C_2H_6$ separations, a number of microporous adsorbents such as $Fe_2(O_2)$(dobdc),[28] Cu(Qc)$_2$,[84] MUF-15,[85] PCN-250,[86] ZIF-7,[87,88] ZIF-8,[89,90] IRMOF-8,[91] Ni(bdc)(ted)$_{0.5}$,[92] MAF-49,[91] CPM-233,[26] and CPM-733[26] adsorb the saturated alkane selectively exploiting the differences in van der Waals interactions, resulting from the higher polarizability of $C_2H_6$. Figure 15a presents the IAST calculations of the $C_2H_6$ uptake $q_2$ versus the separation selectivity $S_{ads}$ of 90/10 $C_2H_4/C_2H_6$ mixture adsorption at 298 K and 100 kPa in four different MOFs. The hierarchy of separation selectivities is Cu(Qc)$_2$ > CPM-733 ≈ MUF-15 > CPM-233. However, because of the higher $C_2H_6$ uptake capacity of CPM-733, the separation

https://dx.doi.org/10.1021/acsomega.0c02218
*ACS Omega* 2020, 5, 16987−17004

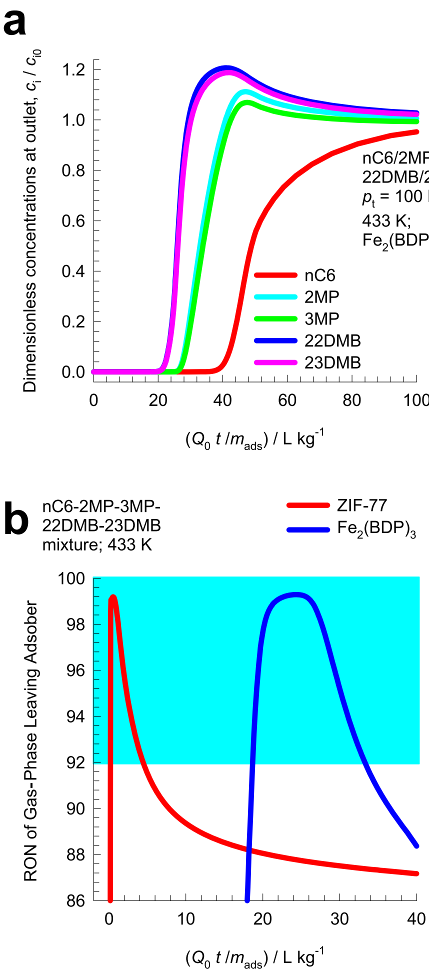

**Figure 17.** (a) Simulations of transient breakthrough characteristics for a five-component $n$C6/2MP/3MP/22DMB/23DMB mixture in a fixed bed adsorber packed with $Fe_2(BDP)_3$ operating at a total pressure of 100 kPa and 433 K. The partial pressures of the components in the bulk gas phase at the inlet are $p_1 = p_2 = p_3 = p_4 = p_5 = 20$ kPa. (b) Plot of RON of product gas mixture exiting the fixed bed adsorber packed with ZIF-77 and $Fe_2(BDP)_3$, plotted as a function of $Q_0t/m_{ads}$. Further information on input data and simulation details are provided in the Supporting Information.

potential, $\Delta q$, follows the hierarchy CPM-733 > CPM-233 > MUF-15 > $Cu(Qc)_2$. The separation potential of $Cu(Qc)_2$ is the lowest because it has the smallest $C_2H_6$ uptake. In order to verify the hierarchy of $\Delta q$ determined from IAST, transient breakthrough simulations were carried out for CPM-733, CPM-233, MUF-15, and $Cu(Qc)_2$; see Figure 15b. The dimensionless concentrations at the exit of the packed bed are plotted as a function of $Q_0t/m_{ads}$. During the interval indicated by the arrows, purified $C_2H_4$ can be recovered. The productivities follow the hierarchy CPM-733 > CPM-233 > MUF-15 > $Cu(Qc)_2$, that is in line with the hierarchy of $\Delta q$ values. From the transient breakthrough simulations, the amount of 99.95%+ pure $C_2H_4$ product recovered during the displacement intervals can be determined. The productivity values show a near-linear dependence on $\Delta q$; see Figure 15c. This implies that the IAST calculations of $\Delta q = q_1y_{20}/y_{10} - q_2$ are appropriate metrics for screening and ranking MOFs.

**2.7. Separation of Hexane Isomers.** The values of the research octane number (RON) of alkane isomers increase with the degree of branching. For hexane isomers, for example, the RON values are $n$-hexane ($n$C6) = 30; 2-methylpentane (2MP) = 74.5; 3-methylpentane (3MP) = 75.5; 2,2 dimethylbutane (22DMB) = 94; and 2,3 dimethylbutane (23DMB) = 105. Consequently, dibranched alkane isomers are preferred blending components in high-octane gasoline.[90,93,94] As shown in the process scheme in Figure 16a, alkane isomers are currently separated on the basis of molecular sieving using LTA-5A zeolite. Linear alkanes can hop from one cage to the adjacent cage through the 4 Å windows of LTA-5A, but monobranched and dibranched alkanes are largely excluded. From an industrial perspective, it is desirable to adopt an alternative separation scheme (see Figure 16b) using an adsorbent that has the capability of separating the dibranched isomers from the linear and monobranched isomers that may be recycled back to the isomerization reactor.

One candidate MOF that can be employed as an adsorbent in Figure 16b is $Fe_2(BDP)_3$ [$BDP^{2-}$ = benzenedipyrazolate] that possesses one-dimensional triangular shape channels of 4.9 Å.[93] Simulations of transient breakthroughs of hexane isomers using $Fe_2(BDP)_3$ are shown in Figure 17a; the hierarchy of breakthroughs is dibranched, monobranched, and linear isomers; this hierarchy is dictated by a combination of adsorption strengths, dictated essentially by van der Waals interactions ($n$C6 ≫ 2MP ≈ 3MP ≫ 22DMB ≈ 23DMB), and diffusivities ($n$C6 > 2MP ≈ 3MP > 22DMB ≈ 23DMB). The RON of the product gas mixture exiting the adsorber is plotted in Figure 17b. During a certain time interval, the 92+ RON product can be recovered for incorporation into the gasoline pool. This requirement of 92+ RON implies that the product stream will contain predominantly the dibranched isomers 22DMB and 23DMB, while allowing a small proportion of 2MP and 3MP to be incorporated into the product stream. Also shown in Figure 17b, for comparison purposes, is the corresponding breakthrough simulation data for ZIF-77[94] that has a characteristic pore dimension of 4.5 Å. Because of stronger diffusional limitations in ZIF-77, the 92+ RON productivity of ZIF-77 is significantly lower than that of $Fe_2(BDP)_3$; this is evidenced by the significantly shorter time interval during which 92+ RON product can be recovered.

**2.8. Separation of C8 Aromatics.** The xylene isomers, $o$-xylene, $m$-xylene, and in particular $p$-xylene, are important chemical intermediates. Xylenes, along with other aromatic hydrocarbons, are commonly obtained from catalytic reforming of naphtha, as illustrated in the process scheme in Figure 18.[63,95,96] The products of catalytic reformer are fed to a distillation column called the reformate splitter. The bottom product of the reformate splitter, rich in xylenes, is further distilled in the xylene splitter, whose bottom product consists of C9+ aromatics. The recovery of $p$-xylene from the mixture of C8 aromatics (typically composition: 20% $o$-xylene, 44% $m$-xylene, 17% $p$-xylene, and 19% ethylbenzene) in the overhead product of the xylene splitter is the focus of attention in this section.

Because of the very small differences in boiling points (cf. Figure 19), $p$-xylene recovery by use of distillation technology is not feasible. Two different technologies are currently in use for recovery of $p$-xylene: (a) fractional crystallization and (b) selective adsorption. Fractional crystallization relies on the differences in freezing points (cf. Figure 19). The freezing point of $p$-xylene is significantly higher than that of other C8 aromatics; on cooling, therefore, pure $p$-xylene crystals are the first to emerge from the solution. Selective adsorption of $p$-xylene from liquid-phase mixtures of C8 aromatics is achieved with cation-exchange FAU zeolite adsorbent, such as BaX, in a

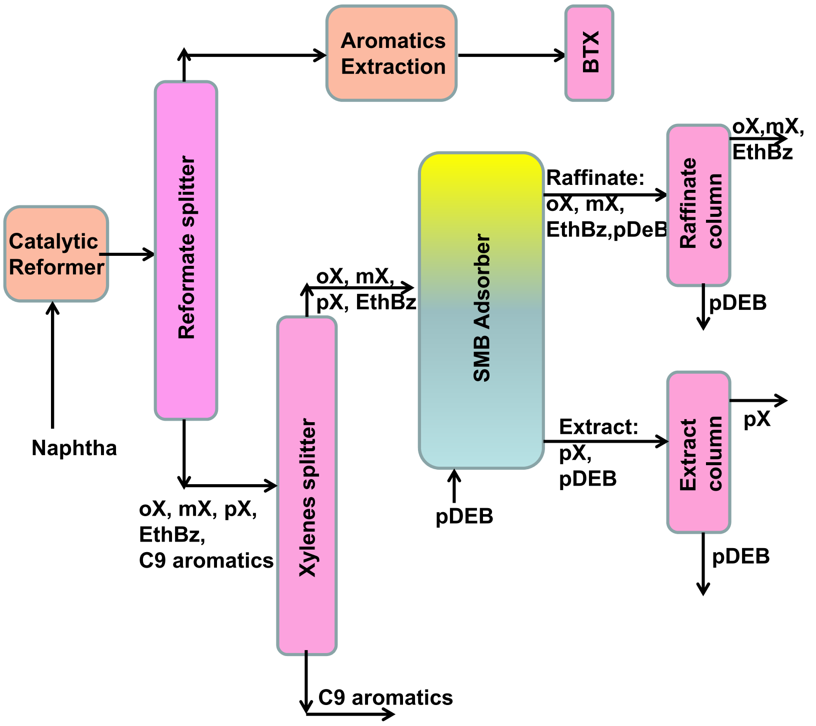

**Figure 18.** Schematic showing the separations of the products from a catalytic reforming unit. Further process background details are provided in the Supporting Information.

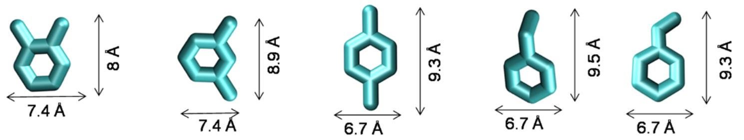

| | o-xylene (oX) | m-xylene (mX) | p-xylene (pX) | Ethylbenzene (EtBz) | Styrene (St) |
|---|---|---|---|---|---|
| Boiling point | 417.6 K | 412.3 K | 411.5 K | 409 K | 418.3 K |
| Freezing point | 248 K | 222 K | 286 K | 178 K | 242.5 K |

**Figure 19.** Boiling points and freezing points of C8 hydrocarbons, along with molecular dimensions, culled from Torres-Knoop et al.[107]

simulated moving bed (SMB) adsorption device.[97−99] The hierarchy of adsorption strengths in BaX is dictated by molecular packing, or entropy, effects that prevail under pore saturation conditions in liquid-phase SMB separations.[95,97−100] Unlike PSA technologies for gaseous separations, the SMB process operates continuously under steady-state conditions; see the schematic in Figure 20.

The C8 aromatic feed is introduced at a port near the middle of the SMB unit.[101,102] The desorbent *p*-diethylbenzene (boiling point 450 K) is introduced at the bottom.[103] Figure 20 also indicates typical liquid phase concentrations of *o*-xylene, *m*-xylene, *p*-xylene, and ethylbenzene along the adsorber height. The extract phase, containing the more strongly adsorbed *p*-xylene, is recovered below the feed injection port in the bottom section of the column. The raffinate phase, containing the more weakly adsorbed *o*-xylene, *m*-xylene, and ethylbenzene, is tapped off above the feed injection port in the upper section of the column.

For realizing improvements in the SMB units, there is considerable scope for the development of MOFs that have both higher uptake capacity and selectivity to *p*-xylene as compared to BaX zeolite. Improved MOF adsorbents will result in lower recirculation flows of eluent, and microporous adsorbent in the SMB unit, and this will result in significant economic advantages. There are several MOFs such as DynaMOF-100,[104,105] Co-CUK-1,[106] MAF-X8,[107] JUC-77,[108] Co(BDP),[21] and MIL-125[109−111] that have the potential for use in SMB units.

For preferential adsorption of *p*-xylene, and rejection of *o*-xylene, *m*-xylene, and ethylbenzene, the appropriate metric for comparing these MOFs is the separation potential $\Delta q$ that is derived using the shock wave model for fixed bed adsorbers[63]

$$\Delta q = (q_{\mathrm{pX}})\frac{y_{\mathrm{oX}} + y_{\mathrm{mX}} + y_{\mathrm{EthBz}}}{1 - y_{\mathrm{oX}} - y_{\mathrm{mX}} - y_{\mathrm{EthBz}}} - (q_{\mathrm{oX}} + q_{\mathrm{mX}} + q_{\mathrm{EthBz}}) \tag{8}$$

In eq 8, the molar loadings of each of the four C8 aromatics, $q_i$, expressed in mol per kilogram of crystalline adsorbent are calculated using the IAST for mixture adsorption equilibrium. Figure 21 presents the plot of $\Delta q$ versus *p*-xylene uptake for a few selected MOFs. The highest value of the separation potential is offered by DynaMOF-100 that is a Zn(II)-based dynamic coordination framework that undergoes guest-induced structural changes so as to allow selective uptake of *p*-xylene

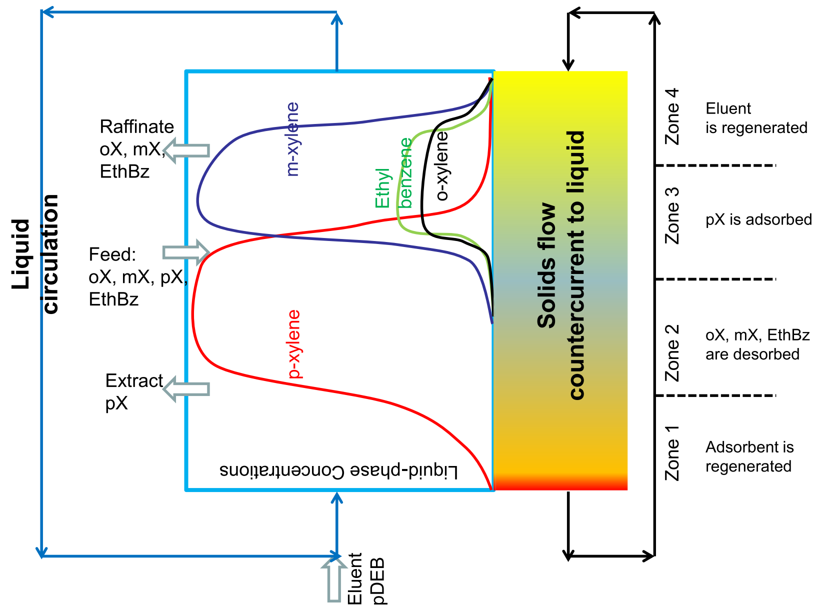

**Figure 20.** SMB adsorption technology for the separation of a feed mixture containing *o*-xylene/*m*-xylene/*p*-xylene/ethylbenzene. The SMB technology is depicted here with countercurrent contacting between the down-flowing adsorbent material and up-flowing desorbent (eluent) liquid. Also indicated are the liquid-phase concentrations of a mixture of *o*-xylene/*m*-xylene/*p*-xylene/ethylbenzene using the information presented by Minceva and Rodrigues.[101]

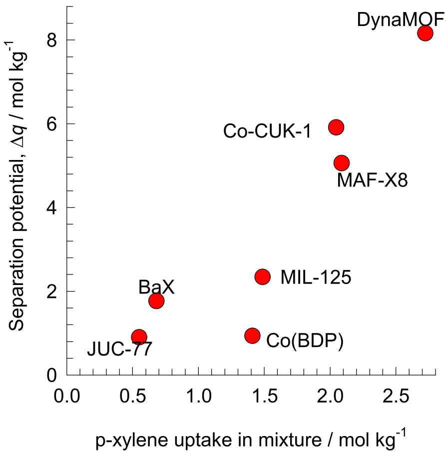

**Figure 21.** Plot of the separation potential, $\Delta q$, vs the gravimetric uptake of *p*-xylene. Further information on input data and simulation details are provided in the Supporting Information.

within the cavities. A slightly lower separation potential is offered by Co-CUK-1 that is composed of cobalt(II) cations and the dianion of dicarboxylic acid; the 1D zigzag-shaped channels of Co-CUK-1 allow optimal vertical stacking of *p*-xylene. Both these MOFs offer separation potentials about three to four times that achievable by BaX; there is a need for experimental verification of this expectation.

**2.9. Influence of Thermodynamic Nonidealities in Mixture Adsorption.** In many cases, the IAST fails to provide a quantitatively correct description of mixture adsorption equilibrium and thus thermodynamic nonidealities come into play. Thermodynamic nonidealities are evidenced for water/alcohol mixtures because of molecular clustering engendered by hydrogen bonding.[112−117] Thermodynamic nonidealities also arise because of preferential location of $CO_2$ molecules at the window regions of eight-ring zeolites such as DDR, CHA, ERI, LTA-4A, and LTA-5A.[55,56,117−119] For $CO_2$ capture with NaX zeolite, there is congregation of $CO_2$ around the cations, resulting in failure of IAST.[117,119] Thermodynamic nonidealities can be strong enough to cause selectivity reversals for $CO_2$/hydrocarbon mixture adsorption in cation-exchanged zeolites.[55,56,117] Framework flexibility and gate-opening behaviors may lead to failure of IAST.[120] In all the aforementioned cases, we need to use the real adsorbed solution theory (RAST) for quantitative description of mixture adsorption in transient breakthrough simulations. RAST calculations of $\Delta q$ may be used for screening purposes.[116,119]

## 3. CONCLUSIONS

The following major conclusions emerge from this study.

(1) The separation performance in fixed bed devices is governed by a combination of adsorption selectivity, $S_{ads}$, and uptake capacities, $q_1$, $q_2$; low uptake capacities diminish the separation performance of MOFs with high values of $S_{ads}$.

(2) The separation potential $\Delta q$, which is calculable on the basis of IAST, provides a simple and convenient metric to screen and rank the separation capability of MOFs. For a component that is recovered in pure form during the adsorption cycle, $\Delta q$ can be calculated using eq 2, which is derived using the shock wave model. For a component that is recovered in pure form during the blowdown cycle, the separation potential $\Delta q$ is defined by eq 7. The value of $\Delta q$ defines the upper limit to the achievable separations in fixed bed units. The actual separations in fixed bed adsorbers will be lower than the IAST-calculated $\Delta q$ values because of distended breakthroughs.

(3) The composition of the feed mixture may have a significant influence on the separation potential of the MOF; this is illustrated in Figure 9c for $C_2H_2$/$C_2H_4$ mixtures.

(4) Broadly speaking, high product purities are more difficult to achieve if the desired product is recovered in the

blowdown cycle of PSA schemes, as presented in Figures 7, 11, and 13. In such cases, it is advantageous to have MOF adsorbents that virtually exclude the less strongly adsorbing component because this facilitates the achievement of high-purity products. The productivity calculations are very sensitive to intracrystalline diffusion limitations, as illustrated in Figure 14 for $C_3H_6/C_3H_8$ mixture separations using KAUST-7.

(5) The concept of separation potential is particularly advantageous for multicomponent separations; several selectivities and uptake capacities are incorporated into one combined metric that quantifies the desired separation task. For example, eq 8 is the appropriate expression for $\Delta q$ for separation of four-component mixture of C8 aromatics

(6) As illustrated in Figures 5, 9, 10, 12, 15, and 17, transient breakthrough experiments or simulations can be directly used to compare the separation effectiveness of MOFs. In such cases, the appropriate *x*-axis for plotting purposes is $Q_0t/m_{\mathrm{ads}}$; this parameter may be viewed as "corrected" time. Such comparisons are indispensable for comparison and screening of MOFs that are subject to severe diffusion limitations,[90,121]

(7) For situations in which the intracrystalline influences are strong, the separation performance will be significantly lowered and IAST calculations of $\Delta q$ will not be adequate for screening purposes.

(8) For kinetically driven separation, as used industrially for $N_2/CH_4$ and $N_2/O_2$ mixtures, some authors have suggested the use of $\sqrt{\text{Đ}_1/\text{Đ}_2}$ as a metric to quantify kinetic influences.[71,81] The concept of the separation potential $\Delta q$ is not of relevance in such cases.

## ■ ASSOCIATED CONTENT

### Supporting Information

The Supporting Information is available free of charge at https://pubs.acs.org/doi/10.1021/acsomega.0c02218.

Methodology used for transient breakthrough simulations, analytic solutions to the shock wave model for fixed bed transient operations, structural information on the MOFs investigated, unary isotherm data sources for each guest/host combination, and data inputs of simulation results for each of the investigated mixture separations (PDF)

## ■ AUTHOR INFORMATION

### Corresponding Author

**Rajamani Krishna** − *Van 't Hoff Institute for Molecular Sciences, University of Amsterdam, 1098 XH Amsterdam, The Netherlands;* orcid.org/0000-0002-4784-8530;
Email: r.krishna@contact.uva.nl

Complete contact information is available at: https://pubs.acs.org/10.1021/acsomega.0c02218

### Notes

The author declares no competing financial interest.

## ■ ACKNOWLEDGMENTS

The simulation code for transient breakthroughs was developed by Dr. Richard Baur and Dr. Jasper van Baten; their assistance and help are gratefully acknowledged.

## ■ NOMENCLATURE

### Latin Alphabet

| | |
|---|---|
| $c_i$ | molar concentration of species *i*, mol $m^{-3}$ |
| $c_{i0}$ | molar concentration of species *i* in fluid mixture at inlet, mol $m^{-3}$ |
| $c_t$ | total molar concentration of mixture, mol $m^{-3}$ |
| $\text{Đ}_i$ | Maxwell−Stefan diffusivity for molecule−wall interaction, $m^2\ s^{-1}$ |
| $L$ | length of packed bed adsorber, m |
| $m_{\mathrm{ads}}$ | mass of adsorbent in packed bed, kg |
| $p_i$ | partial pressure of species *i* in mixture, Pa |
| $p_t$ | total system pressure, Pa |
| $q_i$ | component molar loading of species *i*, mol $kg^{-1}$ |
| $q_t$ | total molar loading in mixture, mol $kg^{-1}$ |
| $Q$ | volumetric flow rate of gas mixture, $m^3\ s^{-1}$ |
| $r_c$ | radius of crystallite, m |
| $S_{\mathrm{ads}}$ | adsorption selectivity, dimensionless |
| $t$ | time, s |
| $T$ | absolute temperature, K |
| $u$ | superficial gas velocity in packed bed, m $s^{-1}$ |
| $v$ | interstitial gas velocity in packed bed, m $s^{-1}$ |
| $y_i$ | mole fraction of species *i* in the bulk fluid phase, dimensionless |
| $z$ | distance along the adsorber, m |

### Greek Alphabet

| | |
|---|---|
| $\varepsilon$ | voidage of packed bed, dimensionless |
| $\rho$ | framework density, kg $m^{-3}$ |
| $\tau$ | time, dimensionless |

## ■ REFERENCES

(1) Sircar, S.; Golden, T. C. Purification of Hydrogen by Pressure Swing Adsorption. *Separ. Sci. Technol.* **2000**, *35*, 667−687.

(2) Ribeiro, A. M.; Grande, C. A.; Lopes, F. V. S.; Loureiro, J. M.; Rodrigues, A. E. A parametric study of layered bed PSA for hydrogen purification. *Chem. Eng. Sci.* **2008**, *63*, 5258−5273.

(3) Banu, A.-M.; Friedrich, D.; Brandani, S.; Düren, T. A Multiscale Study of MOFs as Adsorbents in $H_2$ PSA Purification. *Ind. Eng. Chem. Res.* **2013**, *52*, 9946−9957.

(4) Majlan, E. H.; Wan Daud, W. R.; Iyuke, S. E.; Mohamad, A. B.; Kadhum, A. A. H.; Mohammad, A. W.; Takriff, M. S.; Bahaman, N. Hydrogen purification using compact pressure swing adsorption system for fuel cell. *Int. J. Hydrogen Energy* **2009**, *34*, 2771−2777.

(5) Yang, R. T. *Adsorbents: Fundamentals and Applications*; John Wiley & Sons, Inc.: Hoboken, New Jersey, 2003.

(6) Ruthven, D. M. *Principles of Adsorption and Adsorption Processes*; John Wiley: New York, 1984.

(7) Ruthven, D. M.; Farooq, S.; Knaebel, K. S. *Pressure Swing Adsorption*; VCH Publishers: New York, 1994.

(8) Ahn, S.; You, Y.-W.; Lee, D.-G.; Kim, K.-H.; Oh, M.; Lee, C.-H. Layered Two- and Four-bed PSA Processes for H2 Recovery from Coal Gas. *Chem. Eng. Sci.* **2012**, *68*, 413−423.

(9) Pakseresht, S.; Kazemeini, M.; Akbarnejad, M. M. Equilibrium isotherms for CO, $CO_2$, $CH_4$ and $C_2H_4$ on the 5A molecular sieve by a simple volumetric apparatus. *Sep. Purif. Technol.* **2002**, *28*, 53−60.

(10) Sircar, S. Basic research needs for design of adsorptive gas separation processes. *Ind. Eng. Chem. Res.* **2006**, *45*, 5435−5448.

(11) Yang, R. T. *Gas Separation by Adsorption Processes*; Butterworth: Boston, 1987.

(12) Belmabkhout, Y.; Pirngruber, G.; Jolimaitre, E.; Methivier, A. A complete experimental approach for synthesis gas separation studies using static gravimetric and column breakthrough experiments. *Adsorption* **2007**, *13*, 341−349.

(13) Wu, H.; Yao, K.; Zhu, Y.; Li, B.; Shi, Z.; Krishna, R.; Li, J. Cu-TDPAT, an rht-type Dual-Functional Metal−Organic Framework Offering Significant Potential for Use in $H_2$ and Natural Gas

Purification Processes Operating at High Pressures. *J. Phys. Chem. C* **2012**, *116*, 16609−16618.

(14) Herm, Z. R.; Krishna, R.; Long, J. R. $CO_2/CH_4$, $CH_4/H_2$ and $CO_2/CH_4/H_2$ separations at high pressures using $Mg_2$(dobdc). *Microporous Mesoporous Mater.* **2012**, *151*, 481−487.

(15) Herm, Z. R.; Swisher, J. A.; Smit, B.; Krishna, R.; Long, J. R. Metal-Organic Frameworks as Adsorbents for Hydrogen Purification and Pre-Combustion Carbon Dioxide Capture. *J. Am. Chem. Soc.* **2011**, *133*, 5664−5667.

(16) Mason, J. A.; Sumida, K.; Herm, Z. R.; Krishna, R.; Long, J. R. Evaluating Metal-Organic Frameworks for Post-Combustion Carbon Dioxide Capture via Temperature Swing Adsorption. *Energy Environ. Sci.* **2011**, *4*, 3030−3040.

(17) Xiang, S.; He, Y.; Zhang, Z.; Wu, H.; Zhou, W.; Krishna, R.; Chen, B. Microporous Metal-Organic Framework with Potential for Carbon Dioxide Capture at Ambient Conditions. *Nat. Commun.* **2012**, *3*, 954.

(18) Asgari, M.; Semino, R.; Schouwink, P. A.; Kochetygov, I.; Tarver, J.; Trukhina, O.; Krishna, R.; Brown, C. M.; Ceriotti, M.; Queen, W. L. Understanding how Ligand Functionalization influences $CO_2$ and N2 Adsorption in a Sodalite MOF. *Chem. Mater.* **2020**, *32*, 1526−1536.

(19) Krishna, R.; van Baten, J. M. A comparison of the $CO_2$ capture characteristics of zeolites and metal-organic frameworks. *Sep. Purif. Technol.* **2012**, *87*, 120−126.

(20) Krishna, R. Adsorptive separation of $CO_2/CH_4/CO$ gas mixtures at high pressures. *Microporous Mesoporous Mater.* **2012**, *156*, 217−223.

(21) Krishna, R.; van Baten, J. M. In silico screening of metal-organic frameworks in separation applications. *Phys. Chem. Chem. Phys.* **2011**, *13*, 10593−10616.

(22) Rajagopalan, A. K.; Avila, A. M.; Rajendran, A. Do adsorbent screening metrics predict process performance? Aprocess optimisation based study for post-combustion capture of $CO_2$. *Int. J. Greenhouse Gas Control* **2016**, *46*, 76−85.

(23) Bloch, E. D.; Queen, W. L.; Krishna, R.; Zadrozny, J. M.; Brown, C. M.; Long, J. R. Hydrocarbon Separations in a Metal-Organic Framework with Open Iron(II) Coordination Sites. *Science* **2012**, *335*, 1606−1610.

(24) Cadiau, A.; Adil, K.; Bhatt, P. M.; Belmabkhout, Y.; Eddaoudi, M. A Metal-Organic Framework−Based Splitter for Separating Propylene from Propane. *Science* **2016**, *353*, 137−140.

(25) Lin, R.-B.; Li, L.; Zhou, H.-L.; Wu, H.; He, C.; Li, S.; Krishna, R.; Li, J.; Zhou, W.; Chen, B. Molecular Sieving of Ethylene from Ethane using a Rigid Metal-Organic Framework. *Nat. Mater.* **2018**, *17*, 1128−1133.

(26) Yang, H.; Wang, Y.; Krishna, R.; Jia, X.; Wang, Y.; Hong, A. N.; Dang, C.; Castillo, H. E.; Bu, X.; Feng, P. Pore-Space-Partition-Enabled Exceptional Ethane Uptake and Ethane-Selective Ethane−Ethylene Separation. *J. Am. Chem. Soc.* **2020**, *142*, 2222−2227.

(27) Bao, Z.; Wang, J.; Zhang, Z.; Xing, H.; Yang, Q.; Yang, Y.; Wu, H.; Krishna, R.; Zhou, W.; Chen, B.; Ren, Q. Molecular Sieving of Ethane from Ethylene through the molecular Cross-section Size Differentiation in Gallate-based Metal-Organic Frameworks. *Angew. Chem., Int. Ed.* **2018**, *57*, 16020−16025.

(28) Li, L.; Lin, R.-B.; Krishna, R.; Li, H.; Xiang, S.; Wu, H.; Li, J.; Zhou, W.; Chen, B. Ethane/ethylene Separation in a Metal-Organic Framework with Iron-Peroxo Sites. *Science* **2018**, *362*, 443−446.

(29) Zhang, X.; Li, L.; Wang, J.-X.; Wen, H.-M.; Krishna, R.; Wu, H.; Zhou, W.; Chen, Z.-N.; Li, B.; Qian, G.; Chen, B. Selective Ethane/Ethylene Separation in a Robust Microporous Hydrogen-Bonded Organic Framework. *J. Am. Chem. Soc.* **2020**, *142*, 633−640.

(30) Cui, X.; Chen, K.; Xing, H.; Yang, Q.; Krishna, R.; Bao, Z.; Wu, H.; Zhou, W.; Dong, X.; Han, Y.; Li, B.; Ren, Q.; Zaworotko, M. J.; Chen, B. Pore Chemistry and Size Control in Hybrid Porous Materials for Acetylene Capture from Ethylene. *Science* **2016**, *353*, 141−144.

(31) Peng, Y. L.; He, C.; Pham, T.; Wang, T.; Li, P.; Krishna, R.; Forrest, K. A.; Hogan, A.; Suepaul, S.; Space, B.; Fang, M.; Chen, Y.; Zaworotko, M. J.; Li, J.; Li, L.; Zhang, Z.; Cheng, P.; Chen, B. Robust Microporous Metal-Organic Frameworks for Highly Efficient and Simultaneous Removal of Propyne and Propadiene from Propylene. *Angew. Chem., Int. Ed.* **2019**, *58*, 10209−10214.

(32) Tao, Y.; Krishna, R.; Yang, L. X.; Fan, Y. L.; Wang, L.; Gao, Z.; Xiong, J. B.; Sun, L. J.; Luo, F. Enhancing $C_2H_2/C_2H_4$ separation by incorporating low-content sodium in covalent organic framework. *Inorg. Chem. Front.* **2019**, *6*, 2921−2926.

(33) Li, L.; Wen, H. M.; He, C.; Lin, R. B.; Krishna, R.; Wu, H.; Zhou, W.; Li, J.; Li, B.; Chen, B. A Metal−Organic Framework with Suitable Pore Size and Specific Functional Site for Removal of Trace Propyne from Propylene. *Angew. Chem., Int. Ed.* **2018**, *57*, 15183−15188.

(34) Li, L.; Lin, R.-B.; Krishna, R.; Wang, X.; Li, B.; Wu, H.; Li, J.; Zhou, W.; Chen, B. Efficient Separation of Ethylene from Acetylene/Ethylene Mixtures by a Flexible-Robust Metal−Organic Framework. *J. Mater. Chem. A* **2017**, *5*, 18984−18988.

(35) Li, L.; Lin, R.-B.; Krishna, R.; Wang, X.; Li, B.; Wu, H.; Li, J.; Zhou, W.; Chen, B. Flexible−Robust Metal−Organic Framework for Efficient Removal of Propyne from Propylene. *J. Am. Chem. Soc.* **2017**, *139*, 7733−7736.

(36) Li, L.; Krishna, R.; Wang, Y.; Wang, X.; Yang, J.; Li, J. Flexible metal−organic frameworks with discriminatory gate-opening effect for separation of acetylene from ethylene/acetylene mixtures. *Eur. J. Inorg. Chem.* **2016**, 4457−4462.

(37) Wen, H.-M.; Li, B.; Wang, H.; Wu, C.; Alfooty, K.; Krishna, R.; Chen, B. A Microporous Metal−Organic Framework with Rare lvt Topology for Highly Selective $C_2H_2/C_2H_4$ Separation at Room Temperature. *Chem. Commun.* **2015**, *51*, 5610−5613.

(38) Matsuda, R.; Kitaura, R.; Kitagawa, S.; Kubota, Y.; Belosludov, R. V.; Kobayashi, T. C.; Sakamoto, H.; Chiba, T.; Takata, M.; Kawazoe, Y.; Mita, Y. Highly controlled acetylene accommodation in a metal−organic microporous material. *Nature* **2005**, *436*, 238−241.

(39) Fischer, M.; Hoffmann, F.; Fröba, M. New Microporous Materials for Acetylene Storage and $C_2H_2/CO_2$ Separation: Insights from Molecular Simulations. *ChemPhysChem* **2010**, *11*, 2220−2229.

(40) Wang, L.; Yang, L.; Gong, L.; Krishna, R.; Gao, Z.; Tao, Y.; Yin, W.; Xu, Z.; Luo, F. Constructing redox-active microporous hydrogen-bonded organic framework by imide-functionalization: photochromism, electrochromism, and selective adsorption of $C_2H_2$ over $CO_2$. *Chem. Eng. J.* **2020**, *383*, 123117.

(41) Gao, J.; Qian, X.; Lin, R. B.; Krishna, R.; Wu, H.; Zhou, W.; Chen, B. Mixed Metal-Organic Framework with Multiple Binding Sites for Efficient $C_2H_2/CO_2$ Separation. *Angew. Chem., Int. Ed.* **2020**, *59*, 4396−4400.

(42) Liu, R.; Liu, Q.-Y.; Krishna, R.; Wang, W.; He, C.-T.; Wang, Y.-L. Water-stable Europium-1,3,6,8-tetrakis(4-carboxylphenyl)pyrene Framework for Efficient $C_2H_2/CO_2$ Separation. *Inorg. Chem.* **2019**, *58*, 5089−5095.

(43) Ye, Y.; Ma, Z.; Lin, R.-B.; Krishna, R.; Zhou, W.; Lin, Q.; Zhang, Z.; Xiang, S.; Chen, B. Pore Space Partition within a Metal-Organic Framework for Highly Efficient $C_2H_2/CO_2$ Separation. *J. Am. Chem. Soc.* **2019**, *141*, 4130−4136.

(44) Wu, H. Q.; Yan, C. S.; Luo, F.; Krishna, R. Beyond Crystal Engineering: Significant Enhancement of $C_2H_2/CO_2$ Separation by Constructing Composite Material. *Inorg. Chem.* **2018**, *57*, 3679−3682.

(45) Foo, M. L.; Matsuda, R.; Hijikata, Y.; Krishna, R.; Sato, H.; Horike, S.; Hori, A.; Duan, J.; Sato, Y.; Kubota, Y.; Takata, M.; Kitagawa, S. An Adsorbate Discriminatory Gate Effect in a Flexible Porous Coordination Polymer for Selective Adsorption of $CO_2$ over $C_2H_2$. *J. Am. Chem. Soc.* **2016**, *138*, 3022−3030.

(46) Luo, F.; Yan, C.; Dang, L.; Krishna, R.; Zhou, W.; Wu, H.; Dong, X.; Han, Y.; Hu, T.-L.; O'Keeffe, M.; Wang, L.; Luo, M.; Lin, R.-B.; Chen, B. UTSA-74: A MOF-74 Isomer with Two Accessible Binding Sites per Metal Center for Highly Selective Gas Separation. *J. Am. Chem. Soc.* **2016**, *138*, 5678−5684.

(47) Duan, J.; Jin, W.; Krishna, R. Natural Gas Purification Using a Porous Coordination Polymer with Water and Chemical Stability. *Inorg. Chem.* **2015**, *54*, 4279−4284.

(48) Li, P.; He, Y.; Zhao, Y.; Weng, L.; Wang, H.; Krishna, R.; Wu, H.; Zhou, W.; O'Keeffe, M.; Han, Y.; Chen, B. A Rod-Packing Microporous Hydrogen-Bonded Organic Framework for Highly Selective Separation

of $C_2H_2/CO_2$ at Room Temperature. *Angew. Chem., Int. Ed.* **2015**, *54*, 574−577.

(49) Chen, K.-J.; Scott, H. S.; Madden, D. G.; Pham, T.; Kumar, A.; Bajpai, A.; Lusi, M.; Forrest, K. A.; Space, B.; Perry, J. J.; Zaworotko, M. J. Benchmark $C_2H_2/CO_2$ and $CO_2/C_2H_2$ Separation by Two Closely Related Hybrid Ultramicroporous Materials. *Chem* **2016**, *1*, 753−765.

(50) Lee, J.; Chuah, C. Y.; Kim, J.; Kim, Y.; Ko, N.; Seo, Y.; Kim, K.; Bae, T. H.; Lee, E. Separation of Acetylene from Carbon Dioxide and Ethylene by a Water-Stable Microporous Metal−Organic Framework with Aligned Imidazolium Groups inside the Channels. *Angew. Chem., Int. Ed.* **2018**, *130*, 7995−7999.

(51) Scott, H. S.; Shivanna, M.; Bajpai, A.; Madden, D. G.; Chen, K.-J.; Pham, T.; Forrest, K. A.; Hogan, A.; Space, B.; Perry, J. J., IV; Zaworotko, M. J. Highly Selective Separation of C2H2 from CO2 by a New Dichromate-Based Hybrid Ultramicroporous Material. *ACS Appl. Mater. Interfaces* **2017**, *9*, 33395−33400.

(52) Qazvini, O. T.; Babarao, R.; Telfer, S. G. Multipurpose Metal−Organic Framework for the Adsorption of Acetylene: Ethylene Purification and Carbon Dioxide Removal. *Chem. Mater.* **2019**, *31*, 4919−4926.

(53) Pei, J.; Shao, K.; Wang, J. X.; Wen, H. M.; Yang, Y.; Cui, Y.; Krishna, R.; Li, B.; Qian, G. A Chemically Stable Hofmann-Type Metal−Organic Framework with Sandwich-Like Binding Sites for Benchmark Acetylene Capture. *Adv. Mater.* **2020**, *32*, 1908275.

(54) Bachman, J. E.; Reed, D. A.; Kapelewski, M. T.; Chachra, G.; Jonnavittula, D.; Radaelli, G.; Long, J. R. Enabling alternative ethylene production through its selective adsorption in the metal−organic framework $Mn_2$(m-dobdc). *Energy Environ. Sci.* **2018**, *11*, 2423−2431.

(55) van Zandvoort, I.; Ras, E.-J.; Graaf, R. d.; Krishna, R. Using Transient Breakthrough Experiments for Screening of Adsorbents for Separation of $C_2H_4/CO_2$ Mixtures. *Sep. Purif. Technol.* **2020**, *241*, 116706.

(56) van Zandvoort, I.; van der Waal, J. K.; Ras, E.-J.; de Graaf, R.; Krishna, R. Highlighting non-idealities in $C_2H_4/CO_2$ mixture adsorption in 5A zeolite. *Sep. Purif. Technol.* **2019**, *227*, 115730.

(57) Banerjee, D.; Cairns, A. J.; Liu, J.; Motkuri, R. K.; Nune, S. K.; Fernandez, C. A.; Krishna, R.; Strachan, D. M.; Thallapally, P. K. Potential of Metal-Organic Frameworks for Capture of Noble Gases. *Acc. Chem. Res.* **2015**, *48*, 211−219.

(58) Krishna, R. Diffusing Uphill with James Clerk Maxwell and Josef Stefan. *Chem. Eng. Sci.* **2019**, *195*, 851−880.

(59) Chen, X.; Plonka, A. M.; Banerjee, D.; Krishna, R.; Schaef, H. T.; Ghose, S.; Thallapally, P. K.; Parise, J. B. Direct Observation of Xe and Kr Adsorption in a Xe-selective Microporous Metal Organic Framework. *J. Am. Chem. Soc.* **2015**, *137*, 7007−7010.

(60) Feng, X.; Zong, Z.; Elsaidi, S. K.; Jasinski, J. B.; Krishna, R.; Thallapally, P. K.; Carreon, M. A. Kr/Xe Separation over a Chabazite Zeolite Membrane. *J. Am. Chem. Soc.* **2016**, *138*, 9791−9794.

(61) Wang, H.; Yao, K.; Zhang, Z.; Jagiello, J.; Gong, Q.; Han, Y.; Li, J. The First Example of Commensurate Adsorption of Atomic Gas in a MOF and Effective Separation of Xenon from Other Noble Gases. *Chem. Sci.* **2014**, *5*, 620−624.

(62) Kluge, G.; Franke, T.; Schöllner, R.; Nagel, G. Estimation of Component Loadings in Fixed-Bed Adsorption from Breakthrough Curves of Binary Gas Mixtures in Nontrace Systems. *Chem. Eng. Sci.* **1991**, *46*, 368−371.

(63) Krishna, R. Screening Metal-Organic Frameworks for Mixture Separations in Fixed-Bed Adsorbers using a Combined Selectivity/Capacity Metric. *RSC Adv.* **2017**, *7*, 35724−35737.

(64) Myers, A. L.; Prausnitz, J. M. Thermodynamics of Mixed Gas Adsorption. *AIChE J.* **1965**, *11*, 121−127.

(65) Liu, J.; Thallapally, P. K.; Strachan, D. Metal−Organic Frameworks for Removal of Xe and Kr from Nuclear Fuel Reprocessing Plants. *Langmuir* **2012**, *28*, 11584−11589.

(66) Liu, J.; Strachan, D. M.; Thallapally, P. K. Enhanced noble gas adsorption in Ag@MOF-74Ni. *Chem. Commun.* **2014**, *50*, 466−468.

(67) Gurdal, Y.; Keskin, S. Atomically Detailed Modeling of Metal Organic Frameworks for Adsorption, Diffusion, and Separation of Noble Gas Mixtures. *Ind. Eng. Chem. Res.* **2012**, *51*, 7373−7382.

(68) Li, L.; Yang, J.; Li, J.; Chen, Y.; Li, J. Separation of $CO_2/CH_4$ and $CH_4/N_2$ Mixtures by M/DOBDC: a Detailed Dynamic Comparison with MIL-100(Cr) and Activated Carbon. *Microporous Mesoporous Mater.* **2014**, *198*, 236−246.

(69) Tagliabue, M.; Farrusseng, D.; Valencia, S.; Aguado, S.; Ravon, U.; Rizzo, C.; Corma, A.; Mirodatos, C. Natural gas treating by selective adsorption: Material science and chemical engineering interplay. *Chem. Eng. J.* **2009**, *155*, 553−566.

(70) Bhadra, S. J.; Farooq, S. Separation of MethaneNitrogen Mixture by Pressure Swing Adsorption for Natural Gas Upgrading. *Ind. Eng. Chem. Res.* **2011**, *50*, 14030−14045.

(71) Majumdar, B.; Bhadra, S. J.; Marathe, R. P.; Farooq, S. Adsorption and Diffusion of Methane and Nitrogen in Barium Exchanged ETS-4. *Ind. Eng. Chem. Res.* **2011**, *50*, 3021−3034.

(72) Jayaraman, A.; Hernandez-Maldonado, A. J.; Yang, R. T.; Chinn, D.; Munson, C. L.; Mohr, D. H. Clinoptilolites for Nitrogen/Methane Separation. *Chem. Eng. Sci.* **2004**, *59*, 2407−2417.

(73) Habgood, H. W. The Kinetics of Molecular Sieve Action. Sorption of Nitrogen-Methane Mixtures by Linde Molecular Sieve 4A. *Can. J. Chem.* **1958**, *36*, 1384−1397.

(74) Bhadra, S. J. Methane-Nitrogen Separation by Pressure Swing Adsorption. Ph.D. Dissertation, National University of Singapore, Singapore, 2007.

(75) Yoon, J. W.; Chang, H.; Lee, S.-J.; Hwang, Y. K.; Hong, D.-Y.; Lee, S.-K.; Lee, J. S.; Jang, S.; Yoon, T.-U.; Kwac, K.; Jung, Y.; Pillai, R. S.; Faucher, F.; Vimont, A.; Daturi, M.; Férey, G.; Serre, C.; Maurin, G.; Bae, Y.-S.; Chang, J.-S. Selective Nitrogen Capture by Porous Hybrid Materials Containing Accessible Transition Metal Ion Sites. *Nat. Mater.* **2017**, *16*, 526−531.

(76) Da Silva, F. A.; Rodrigues, A. E. Vacuum swing adsorption for propylene/propane separation with 4A zeolite. *Ind. Eng. Chem. Res.* **2001**, *40*, 5758−5774.

(77) Grande, C. A.; Poplow, F.; Rodrigues, A. E. Vacuum pressure swing adsorption to produce polymer-grade polypropylene. *Separ. Sci. Technol.* **2010**, *45*, 1252−1259.

(78) Silva, F. A. D.; Rodrigues, A. E. PropylenePropane Separation by Vacuum Swing Adsorption Using 13X Zeolite. *AIChE J.* **2001**, *47*, 341−357.

(79) Geier, S. J.; Mason, J. A.; Bloch, E. D.; Queen, W. L.; Hudson, M. R.; Brown, C. M.; Long, J. R. Selective adsorption of ethylene over ethane and propylene over propane in the metal−organic frameworks $M_2$(dobdc) (M = Mg, Mn, Fe, Co, Ni, Zn). *Chem. Sci.* **2013**, *4*, 2054−2061.

(80) Yoon, J.-W.; Jang, I.-T.; Lee, K.-Y.; Hwang, Y.-K.; Chang, J.-S. Adsorptive Separation of Propylene and Propane on a Porous Metal-Organic Framework, Copper Trimesate. *Bull. Korean Chem. Soc.* **2010**, *31*, 220−223.

(81) Khalighi, M.; Karimi, I. A.; Farooq, S. Comparing SiCHA and 4A Zeolite for Propylene/Propane Separation using a Surrogate-Based Simulation/Optimization Approach. *Ind. Eng. Chem. Res.* **2014**, *53*, 16973−16983.

(82) Khalighi, M.; Chen, Y. F.; Farooq, S.; Karimi, I. A.; Jiang, J. W. Propylene/Propane Separation Using SiCHA. *Ind. Eng. Chem. Res.* **2013**, *52*, 3877−3892.

(83) Ruthven, D. M.; Farooq, S. Air Separation by Pressure Swing Adsorption. *Gas Sep. Purif.* **1990**, *4*, 141−148.

(84) Lin, R.-B.; Wu, H.; Li, L.; Tang, X.-L.; Li, Z.; Gao, J.; Cui, H.; Zhou, W.; Chen, B. Boosting Ethane/Ethylene Separation within Isoreticular Ultramicroporous Metal−Organic Frameworks. *J. Am. Chem. Soc.* **2018**, *140*, 12940−12946.

(85) Qazvini, O. T.; Babarao, R.; Shi, Z.-L.; Zhang, Y.-B.; Telfer, S. G. A Robust Ethane-Trapping Metal−Organic Framework with a High Capacity for Ethylene Purification. *J. Am. Chem. Soc.* **2019**, *141*, 5014−5020.

(86) Chen, Y.; Qiao, Z.; Wu, H.; Lv, D.; Shi, R.; Xia, Q.; Zhou, J.; Li, Z. An Ethane-trapping MOF PCN-250 for Highly Selective Adsorption of Ethane over Ethylene. *Chem. Eng. Sci.* **2018**, *175*, 110−117.

(87) Gücüyener, C.; van den Bergh, J.; Gascon, J.; Kapteijn, F. Ethane/Ethene Separation Turned on Its Head: Selective Ethane

Adsorption on the Metal-Organic Framework ZIF-7 through a Gate-Opening Mechanism. *J. Am. Chem. Soc.* **2010**, *132*, 17704−17706.

(88) Chen, D.-L.; Wang, N.; Xu, C.; Tu, G.; Zhu, W.; Krishna, R. A combined theoretical and experimental analysis on transient breakthroughs of C2H6/C2H4 in fixed beds packed with ZIF-7. *Microporous Mesoporous Mater.* **2015**, *208*, 55−65.

(89) Böhme, U.; Barth, B.; Paula, C.; Kuhnt, A.; Schwieger, W.; Mundstock, A.; Caro, J.; Hartmann, M. Ethene/Ethane and Propene/Propane Separation via the Olefin and Paraffin Selective Metal−Organic Framework Adsorbents CPO-27 and ZIF-8. *Langmuir* **2013**, *29*, 8592−8600.

(90) Krishna, R. The Maxwell-Stefan Description of Mixture Diffusion in Nanoporous Crystalline Materials. *Microporous Mesoporous Mater.* **2014**, *185*, 30−50.

(91) Liao, P.-Q.; Zhang, W.-X.; Zhang, J.-P.; Chen, X.-M. Efficient purification of ethene by an ethane-trapping metal-organic framework. *Nat. Commun.* **2015**, *36*, 8697.

(92) Liang, W.; Xu, F.; Zhou, X.; Xiao, J.; Xia, Q.; Li, Y.; Li, Z. Ethane Selective Adsorbent Ni(bdc)(ted)0.5 with High Uptake and its Significance in Adsorption Separation of Ethane and Ethylene. *Chem. Eng. Sci.* **2016**, *148*, 275−281.

(93) Herm, Z. R.; Wiers, B. M.; Mason, J. A.; van Baten, J. M.; Hudson, M. R.; Zajdel, P.; Brown, C. M.; Masciocchi, N.; Krishna, R.; Long, J. R. Separation of Hexane Isomers in a Metal-Organic Framework with Triangular Channels. *Science* **2013**, *340*, 960−964.

(94) Dubbeldam, D.; Krishna, R.; Calero, S.; Yazaydın, A. Ö. Computer-Assisted Screening of Ordered Crystalline Nanoporous Adsorbents for Separation of Alkane Isomers. *Angew. Chem., Int. Ed.* **2012**, *51*, 11867−11871.

(95) Krishna, R. Separating Mixtures by Exploiting Molecular Packing Effects in Microporous Materials. *Phys. Chem. Chem. Phys.* **2015**, *17*, 39−59.

(96) Krishna, R. Methodologies for Screening and Selection of Crystalline Microporous Materials in Mixture Separations. *Sep. Purif. Technol.* **2018**, *194*, 281−300.

(97) Khabzina, Y.; Laroche, C.; Perez-Pellitero, J.; Farrusseng, D. Xylene Separation on a Diverse Library of Exchanged Faujasite Zeolites. *Microporous Mesoporous Mater.* **2017**, *247*, 52−59.

(98) Khabzina, Y.; Laroche, C.; Pérez-Pellitero, J.; Farrusseng, D. Quantitative Structure−property Relationship Approach to Predicting Xylene Separation with Diverse Exchanged Faujasites. *Phys. Chem. Chem. Phys.* **2018**, *20*, 23773−23782.

(99) Costa, I. C. M. Adsorption/diffusion Interplay in Hierarchical Zeolites: Understanding the role of External Surface and Additional Porosity. Ph.D. Thesis, l'Université Claude Bernard Lyon 1, Lyon, 2019.

(100) Krishna, R.; van Baten, J. M. Commensurate-Incommensurate Adsorption and Diffusion in Ordered Crystalline Microporous Materials. *Phys. Chem. Chem. Phys.* **2017**, *19*, 20320−20337.

(101) Minceva, M.; Rodrigues, A. E. Modeling and Simulation of a Simulated Moving Bed for the Separation of p-Xylene. *Ind. Eng. Chem. Res.* **2002**, *41*, 3454−3461.

(102) Minceva, M.; Rodrigues, A. E. Understanding and Revamping of Industrial Scale SMB Units for p-Xylene Separation. *AIChE J.* **2007**, *53*, 138−149.

(103) Kulprathipanja, S. *Zeolites in Industrial Separation and Catalysis*; Wiley-VCH: Weinheim, 2010.

(104) Mukherjee, S.; Joarder, B.; Manna, B.; Desai, A. V.; Chaudhari, A. K.; Ghosh, S. K. Framework-Flexibility Driven Selective Sorption of p-Xylene over Other Isomers by a Dynamic Metal-Organic Framework. *Sci. Rep.* **2015**, *4*, 5761.

(105) Mukherjee, S.; Joarder, B.; Desai, A. V.; Manna, B.; Krishna, R.; Ghosh, S. K. Exploiting Framework Flexibility of a Metal-Organic Framework for Selective Adsorption of Styrene over Ethylbenzene. *Inorg. Chem.* **2015**, *54*, 4403−4408.

(106) Yoon, J. W.; Lee, J. S.; Piburn, G. W.; Cho, K. H.; Jeon, K.; Lim, H.-K.; Kim, H.; Jun, C.-H.; Humphrey, S. M.; Krishna, R.; Chang, J.-S. Highly Selective Adsorption of p-Xylene over other C8 Aromatic Hydrocarbons by Co-CUK-1: A Combined Experimental and Theoretical Assessment. *Dalton Trans.* **2017**, *46*, 16096−16101.

(107) Torres-Knoop, A.; Krishna, R.; Dubbeldam, D. Separating Xylene Isomers by Commensurate Stacking of p-Xylene within Channels of MAF-X8. *Angew. Chem., Int. Ed.* **2014**, *53*, 7774−7778.

(108) Jin, Z.; Zhao, H.-Y.; Zhao, X.-J.; Fang, Q.-R.; Long, J. R.; Zhu, G.-S. A novel microporous MOF with the capability of selective adsorption of xylenes. *Chem. Commun.* **2010**, *46*, 8612−8614.

(109) Moreira, M. A.; Santos, J. C.; Ferreira, A. F. P.; Loureiro, J. M.; Ragon, F.; Horcajada, P.; Yot, P. G.; Serre, C.; Rodrigues, A. E. Toward Understanding the Influence of Ethylbenzene in p-Xylene Selectivity of the Porous Titanium Amino Terephthalate MIL-125(Ti): Adsorption Equilibrium and Separation of Xylene Isomers. *Langmuir* **2012**, *28*, 3494−3502.

(110) Moreira, M. A.; Santos, J. C.; Ferreira, A. F. P.; Loureiro, J. M.; Ragon, F.; Horcajada, P.; Yot, P. G.; Serre, C.; Rodrigues, A. E. Effect of ethylbenzene in p-xylene selectivity of the porous titanium amino terephthalate MIL-125(Ti)_NH2. *Microporous Mesoporous Mater.* **2012**, *158*, 229−234.

(111) Vermoortele, F.; Maes, M.; Moghadam, P. Z.; Lennox, M. J.; Ragon, F.; Boulhout, M.; Biswas, S.; Laurier, K. G. M.; Beurroies, I.; Denoyel, R.; Roeffaers, M.; Stock, N.; Düren, T.; Serre, C.; De Vos, D. E. p-Xylene-Selective MetalOrganic Frameworks: A Case of Topology-Directed Selectivity. *J. Am. Chem. Soc.* **2011**, *133*, 18526−18529.

(112) Krishna, R.; van Baten, J. M. Highlighting a variety of unusual characteristics of adsorption and diffusion in microporous materials induced by clustering of guest molecules. *Langmuir* **2010**, *26*, 8450−8463.

(113) Krishna, R.; van Baten, J. M. Hydrogen Bonding Effects in Adsorption of Water-alcohol Mixtures in Zeolites and the Consequences for the Characteristics of the Maxwell-Stefan Diffusivities. *Langmuir* **2010**, *26*, 10854−10867.

(114) Gutiérrez-Sevillano, J. J.; Calero, S.; Krishna, R. Selective Adsorption of Water from Mixtures with 1-Alcohols by Exploitation of Molecular Packing Effects in CuBTC. *J. Phys. Chem. C* **2015**, *119*, 3658−3666.

(115) Gutiérrez-Sevillano, J. J.; Calero, S.; Krishna, R. Separation of Benzene from Mixtures with Water, Methanol, Ethanol, and Acetone: Highlighting Hydrogen Bonding and Molecular Clustering Influences in CuBTC. *Phys. Chem. Chem. Phys.* **2015**, *17*, 20114−20124.

(116) Krishna, R.; van Baten, J. M.; Baur, R. Highlighting the Origins and Consequences of Thermodynamic Nonidealities in Mixture Separations using Zeolites and Metal-Organic Frameworks. *Microporous Mesoporous Mater.* **2018**, *267*, 274−292.

(117) Krishna, R.; Van Baten, J. M. Elucidation of Selectivity Reversals for Binary Mixture Adsorption in Microporous Adsorbents. *ACS Omega* **2020**, *5*, 9031−9040.

(118) Krishna, R.; van Baten, J. M. Segregation effects in adsorption of $CO_2$ containing mixtures and their consequences for separation selectivities in cage-type zeolites. *Sep. Purif. Technol.* **2008**, *61*, 414−423.

(119) Krishna, R.; Van Baten, J. M. Investigating the Non-idealities in Adsorption of $CO_2$-bearing Mixtures in Cation-exchanged Zeolites. *Sep. Purif. Technol.* **2018**, *206*, 208−217.

(120) Fraux, G.; Boutin, A.; Fuchs, A. H.; Coudert, F.-X. On the Use of the IAST Method for Gas Separation Studies in Porous Materials with Gate-opening Behavior. *Adsorption* **2018**, *24*, 233−241.

(121) Krishna, R. Methodologies for Evaluation of Metal-Organic Frameworks in Separation Applications. *RSC Adv.* **2015**, *5*, 52269−52295.

(122) Krishna, R.; Long, J. R. Screening metal-organic frameworks by analysis of transient breakthrough of gas mixtures in a fixed bed adsorber. *J. Phys. Chem. C* **2011**, *115*, 12941−12950.